# Environment-imposed constraints can make Brownian walkers efficient searchers

Harshana Rajakaruna[1], James O'Connor[2], Ian A. Cockburn[2] and Vitaly V. Ganusov[1,*]

[1]Department of Microbiology, University of Tennessee, Knoxville, TN 37996, USA
[2]Department of Immunology and Infectious Disease, John Curtin School of Medical Research, Australian National University, Canberra, 2601, Australia
[*]Corresponding author: vitaly.ganusov@gmail.com

December 13, 2020

**Abstract**

Pathogen-specific CD8 T cells face the problem of finding rare cells that present their cognate antigen either in the lymph node or infected tissue. To optimize the search for rare targets it has been proposed that T cells might perform a random walk with long displacements called Levy walks enabling superdiffusive behavior and shorter search times[1–3]. Many agents ranging from cells to large animals have been found to perform Levy walks[3–5] suggesting that Levy walk-based search strategies may be evolutionary selected[6,7]. However, whether random walk patterns are driven by agent-intrinsic programs or shaped by environmental factors remains largely unknown[8]. To address this problem we examined the behavior of activated CD8 T cells in the liver where both the movement of the cells and the underlying structural constraints can be clearly defined. We show that *Plasmodium*-specific liver-localized CD8 T cells perform short displacement, Brownian-like walks and yet display transiently superdiffusive displacement, the cardinal feature of efficient Levy walks. Because liver-localized CD8 T cells are mainly associated with liver sinusoids, simulations of Brownian or Levy walkers in structures derived from the liver sinusoids illustrate that structure together with preferred forward movement results in superdiffusive movement. Interestingly, Brownian walkers require less time to find a rare target when T cells search for the infection in physiologically-derived liver structures. Importantly, analysis of fibroblastic reticular cell networks on which CD8 T cells move in lymph nodes also allows for superdiffusion in simulations, though this is not observed experimentally, suggesting that structure is not the only factor determining movement patterns of T cells. Our results strongly suggest that observed patterns of movement of CD8 T cells are likely to result from a combination of a cell-intrinsic movement program, physical constraints imposed by the environmental structures, and other environmental cues. Future work needs to focus on quantifying the relative contributions of these factors to the overall observed movement patterns of biological agents.

## Introduction & Results

For adequate protection the adaptive immune system of vertebrates needs to efficiently survey tissues for infection. However, how such efficiency is achieved remains poorly understood. In lymph nodes

naive T cells seem to search randomly for antigen-presenting cells, acting as Brownian walkers, although some role of attracting chemokines has been proposed[9–11]. Even less information exists on infection search strategies in peripheral, nonlymphoid tissues. In the skin, activated or memory CD8 T cells tend to perform Brownian walks[12], and in explanted murine lungs T cells display intermittent migration resulting in normal diffusion and a large variability in average velocities between individual cells[13]. Surprisingly, *Toxoplasma gondii*-specific activated CD8 T cells in murine brains undergo Levy walks — while most displacements are small, sometimes T cells displace far from the initial location with mean squared displacement increasing faster than linear with time[3]. Levy walks may allow T cells in the brain to locate rare parasite-infected cells efficiently[3,7].

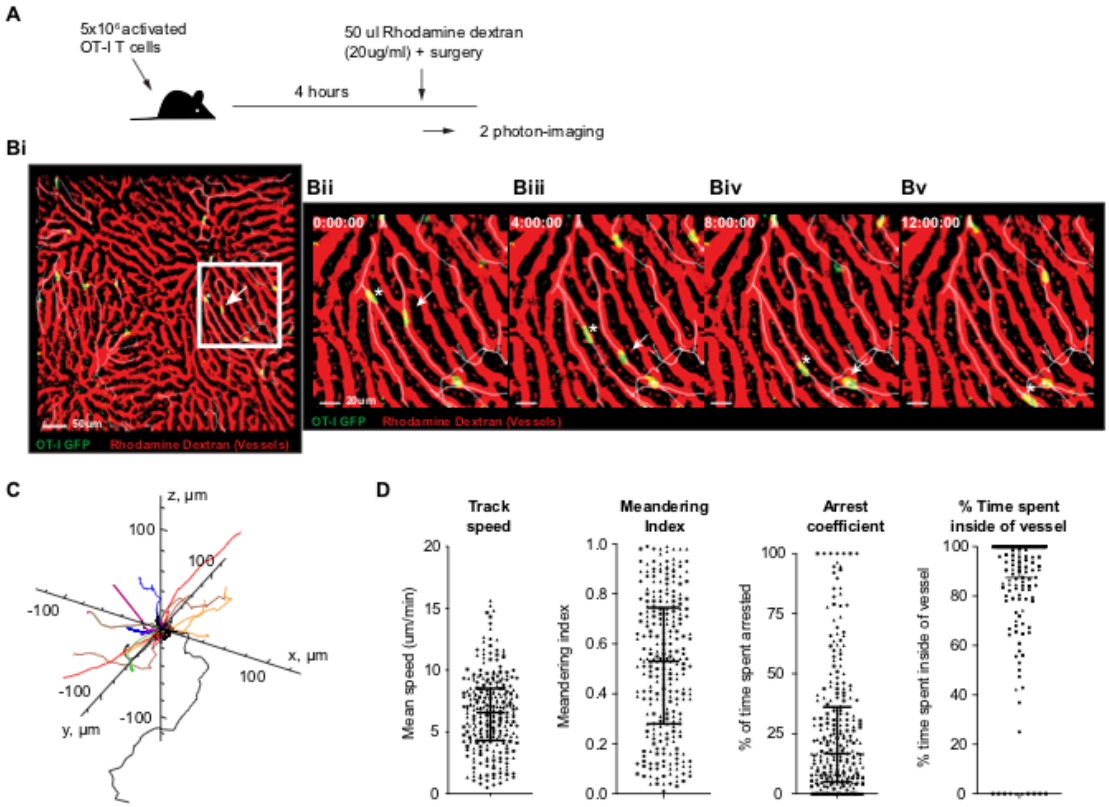


**Figure 1:** The majority of *in vitro* activated CD8 T cells transferred to naive recipients move in liver sinusoids. We performed intravital imaging of the livers of mice that had previously received *in vitro* activated CD8 T cells and i.v. injection of rhodamine dextran (see Materials and Methods for more detail). (A) 4 hours after i.v. cell transfer of $5 \times 10^6$ OT-I GFP CD8 T-lymphocytes (green), mice were injected with 50 µl (20 µg/ml) of rhodamine dextran 70kDa (red) and immediately prepared for intravital imaging. The mice were imaged using a two-photon microscopy with a standard galvanometer scanner in order to acquire a 50 µm deep z-stack. (B) A sequence of images taken over time to demonstrate the movement of GFP cells (green) through the sinusoids (red) in the direction indicated by the white lines (Movie S1) with star and arrow indicating displacement of two different cells. We show the overall scanned area (Bi) and time lapse for 2 cells (indicated by an arrow and a star) moving in the sinusoids (Bii-Bv). Scale bar is 50 µm (Bi) or 20 µm (Bii-Bv). Time in min:sec:milliseconds is shown. (C) Tracks of randomly chosen 30 cells are shown. (D) Movement parameters of OT-I GFP cells in the liver sinusoids such as average track speed, meandering index, and arrest coefficient ($n = 269$). For every cell movement we calculated the percent of time each cell spent in the sinusoids by calculating signal overlap between cell fluorescence (GFP) and sinusoid fluorescence (rhodamine dextran, $n = 231$). The imaging data in B is representative of 3 experiments, and analysis shown in D is for datasets pooled together (means and SD are shown by bars).

Another apicomplexan parasite *Plasmodium*, the causative agents of malaria infects the liver following inoculation of parasites by probing mosquitoes[14,15]. At this stage of the *Plasmodium* lifecycle the intracellular liver stage parasites are susceptible to clearance by vaccine-induced CD8

T cells. Remarkably, liver-localized CD8 T cells alone are capable of eliminating all liver stages and preventing clinical malaria[16,17]. Given that a murine liver has about $10^8$ hepatocytes how exactly CD8 T cells locate all parasites within the 48 hour span of the parasite liver stages is unknown[18].

To understand what strategies *Plasmodium*-specific CD8 T cells may be using to survey the liver for infection we have established a protocol to generate stable numbers of liver-localized CD8 T cells[19]. In these experiments, naive T cells are activated *in vitro*, and then transferred i.v. into naive mice that either left uninfected or can be later infected with *Plasmodium* sporozoites (Fig. 1A)[19]. By injecting fluorescent label (rhodamine-dextran) i.v. immediately prior to surgery and imaging we can efficiently label the liver sinusoids (Fig. 1B). Intravital imaging showed that CD8 T cells in the liver are highly motile cells with the average speed of 6.6 $\mu$m/min, a high meandering index of 0.52, and a low arrest coefficient of 0.25 (Fig. 1C and Movie S1). Importantly, these liver CD8 T cells were observed to be located in liver sinusoids most of the time (89-100%, Fig. 1D). Due to incomplete labeling of the sinusoids and reduced red signal from deeper liver areas it is likely that this is an underestimate and in this system nearly all T cell movements were associated with the sinusoids. A relatively low average speed of these liver-localized T cells and previous experiments with high frequency intravital imaging suggests that the cells are crawling on the endothelial wall of the sinusoids and not flowing with the blood[19]. Thus, our robust experimental set-up allows for the first time to accurately quantify movement patterns of tissue-associated CD8 T cells along with the well defined structures (i.e., hepatic sinusoids) constraining and defining walking patterns of T cells.

In our experiments movements of liver-localized *Plasmodium*-specific CD8 T cells were recorded with two photon microscopy. Interestingly, T cells in the liver displayed transiently superdiffusive displacement ($\gamma > 1$) with $\gamma = 1.64$ for up to 20 min (Fig. 2A). (Saturation in mean squared displacement (MSD) with time in these experiments arose in part due to rapidly moving T cells leaving the imaging area (Fig. S1).) Superdiffusion is a hallmark feature of Levy walks[11,20] but surprisingly, analysis of T cell movement lengths suggested that there were no large displacements (Fig. 2B). Rare but long displacements are the cardinal feature of Levy walks[3,21,22]. Indeed, tail analysis[23] of the distribution of actual or scaled displacements (displacements normalized by the root mean squared displacement, RMSD) suggested the shape parameter of the powerlaw distribution $\mu = 5.6$ — an indication of Brownian ($\mu > 3$) and not Levy ($\mu \leq 3$) walk. In this case it appears that large overall cell displacements with small movement lengths arose not due to Levy-like cell-intrinsic behavior but due to small turning angles and a strong correlation between initial and subsequent velocity vectors for at least 10-15 min, resulting in cells moving in one direction for substantial periods of time (i.e., correlated random walk, Fig. S2).

To complement the movement length distribution tail analysis we fitted a series of alternative mathematical models characterizing the distribution of movement lengths of T cells and found that generalized Pareto distribution fitted the data with best quality (Fig. 2C-D and Tab. S2). Best fit parameters of the generalized Pareto distribution predicted a finite mean and variance for the movement length distribution – which again are the chief features of the Brownian walkers[22]. Thus, analysis of movement data suggests that liver-localized CD8 T cells are Brownian walkers that display transient superdiffusive behavior.

To verify that this result was not due to a potential impact of the injected rhodamine-dextran dye we analyzed four other datasets from our previous study on movement of liver-localized CD8 T cells[19]. These experiments involved transfer of *in vitro* generated wild-type and LFA-1-deficient activated CD8 T cells or *in vivo* generation of liver-localized T cells by transfer of naive OT-I cells to mice followed by immunization of these mice with radiation-attenuated malaria sporozoites (RAS) expressing the SIINFEKL epitope recognized by these cells[18,19]. Both *in vitro* wild-type activated

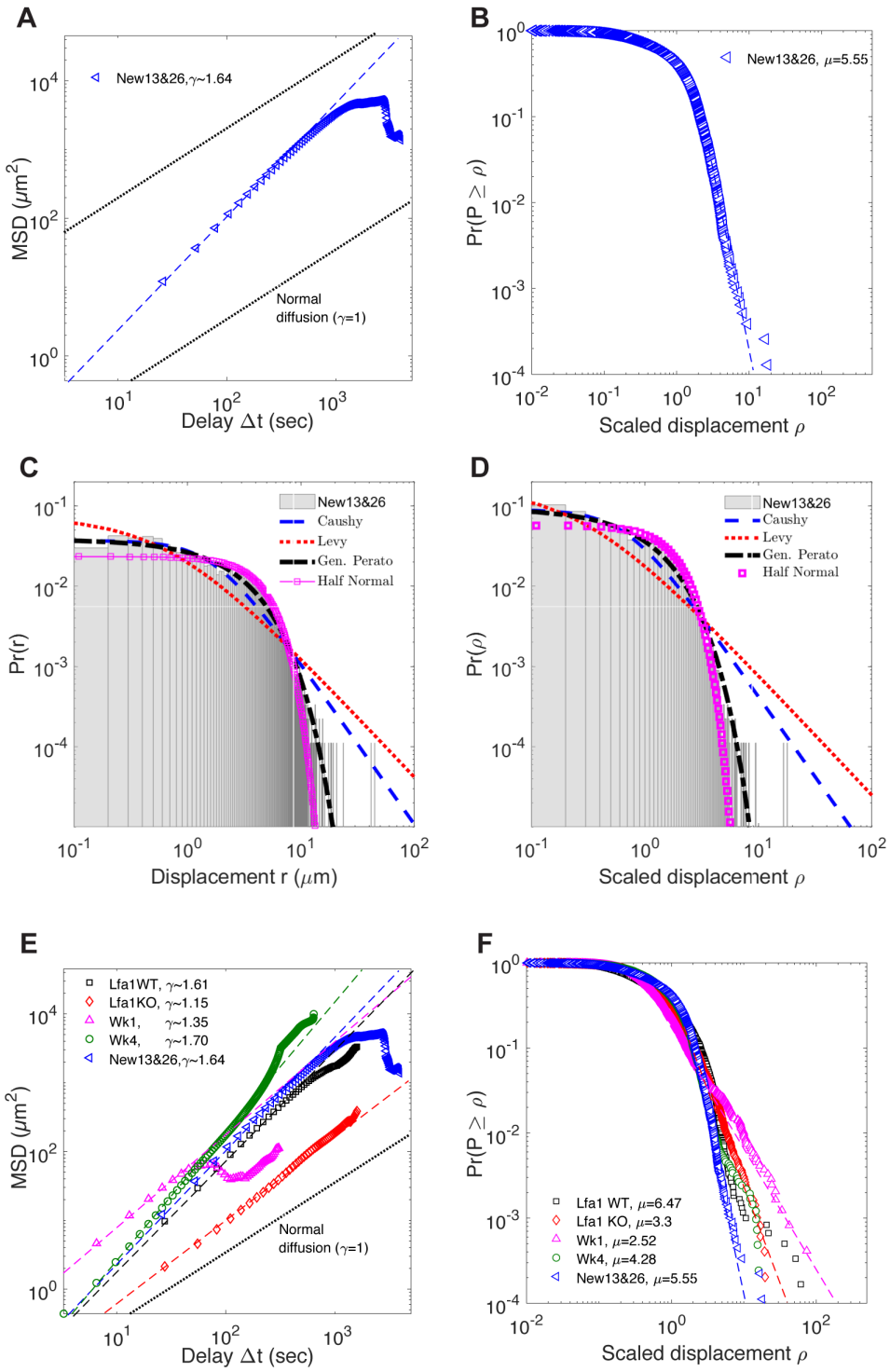


**Figure 2:** Activated CD8 T cells in the liver are Brownian walkers displaying super-diffusive displacement. For experiments described in Fig. 1 we calculated basic movement characteristics such as the mean squared displacement (MSD, A) and distribution of scaled movement lengths (B) for all T cells ($n = 268$). Resulting slopes for linear regressions for the log(MSD) with $\log(t)$ and movement length distribution ($\gamma$ and $\mu$, respectively) are shown on individual panels. Scaling in (B) was done for every track by calculating the root mean squared displacement per cell $\zeta = \sqrt{\overline{\Delta r^2}}$ and calculating a scaled displacement $\rho(t) = r(t)/\zeta$ (see Materials and Methods for detail). (C)-(D). We fit several alternative models of movement length distribution to the raw (C) or scaled (D) displacement data from experiments in Fig. 1 (eqns. (S.4)–(S.9)). Parameters for the fitted models along with AIC values are given in Tabs. S1 and S2. (E)-(F). We performed similar analyses with other published data for *in vitro* or *in vivo* activated CD8 T cells in the liver[19]. Cell displacement in the liver was characterized by MSD with slope $\gamma$ (E) and movement lengths characterized by the tail slope $\mu$ (F). Additional details on analysis of movement length distribution are given in Fig. S3.

cells and *in vivo* activated cells imaged at a memory timepoint (4 weeks) after immunization also displayed transiently superdiffusive behavior with $\gamma > 1$ for 10-20 min. Interestingly, LFA1-deficient T cells which cannot strongly attach to endothelial cells and roll under the blood pressure[19], displayed displacement closest to Brownian and yet being super-diffusive ($\gamma = 1.18$ in Fig. 2E). We also observed high heterogeneity in MSD in mice imaged one week after RAS immunization (Fig. 2E). At this timepoint after *in vivo* priming, many CD8 T cells do not undertake the crawling behavior characteristic of liver-localized T cells, most likely due to intermediate expression of LFA-1 shortly after immunization[19].

Likewise all but one cell population had relatively small movement lengths. The exception was for CD8 T cells in mice one week post RAS immunization (Fig. 2F) where cells do not attach firmly to the liver and endothelium and often flow in the bloodstream[19]. Superdiffusive behavior with relatively small movement lengths was also observed for *Plasmodium*-specific activated CD8 T cells and activated CD8 T cells with irrelevant specificity in *Plasmodium berghei*-infected mice (Fig. S4). Taken together, our results establish that crawling liver-localized CD8 T cells display superdiffusive behavior despite making only small movements in short time intervals.

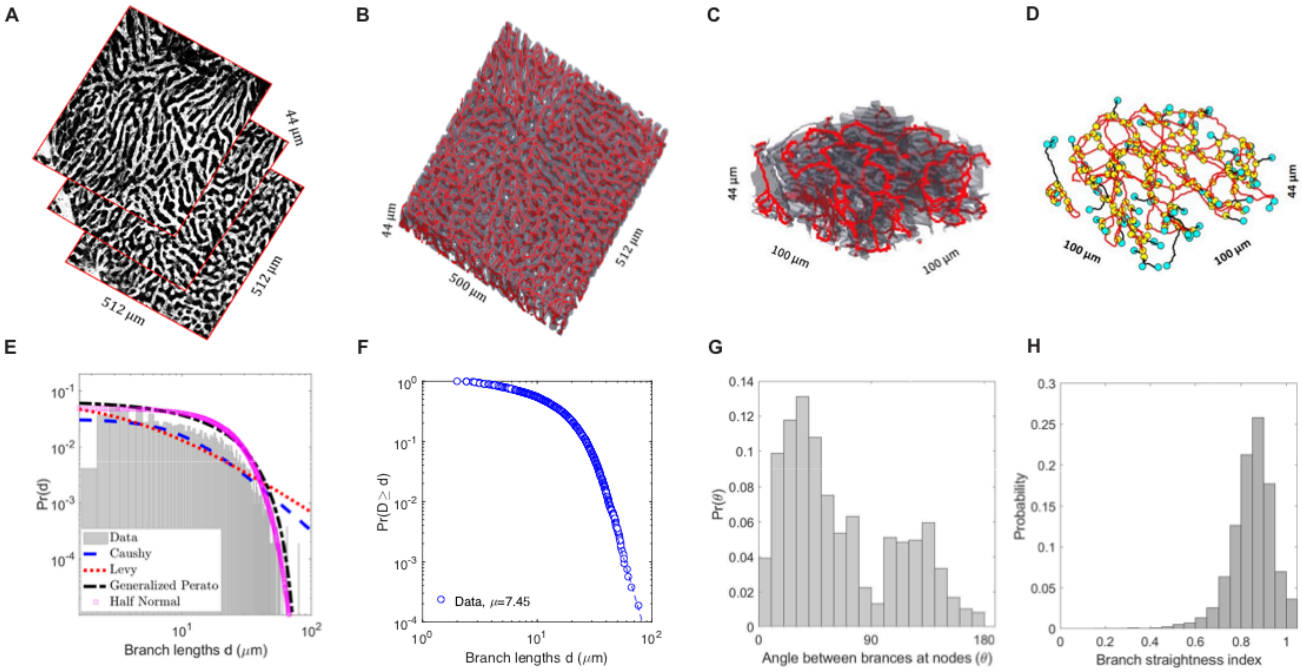


**Figure 3:** Liver sinusoids have relatively short lengths and small branching angles. We performed experiments in which liver sinusoids were labeled by i.v. injection of Evans blue or rhodamine dextran and then imaged immediately by using intravital microscopy. (A) Z-stacks of 2D images of the liver used for analysis. (B) Computer-digitized 3D sinusoidal maps were generated by contrast thresholding and by stacking up the 2D images. Red shows the center paths of the sinusoids. (C)-(D) Computer-assisted rendering of liver sinusoids for a subset of the data (C, shown in red) used to determine the nodes (D, yellow circles) and the edges/branches (red) of the structure (turquoise circles are the end points). (E)-(H) Characterization of the liver sinusoids. (E) We fit several alternative models to the distribution of lengths of sinusoids using likelihood approach (see Materials and Methods and Tab. S1). (F) Cumulative distribution of the sinusoid lengths was also analyzed using tail analysis with the indicated linear regression slope $\mu$[23]. (G) Distribution of branching angles between sinusoids calculated for nodes ($n = 4013$) in D. (H) Straightness of the liver sinusoids (computed as the ratio of point-to-point branch length to actual branch length for all near neighbors in D).

Given the network structure of liver sinusoids (Fig. 1B) and universal pattern of superdiffusive behavior of liver-localized CD8 T cells we hypothesized that a linear structure of the sinusoids may be forcing T cells to move in one direction. Therefore, we analyzed 3D structure of liver sinusoids. For these intravital imaging experiments we injected a contrast dye (Evans blue or rhodamine-dextran)

and imaged murine livers (Fig. 3A). Z-stacks of the images were processed in Matlab to generate highlighted sinusoidal maps (Fig. 3B). A subset of the full image was further processed to generate nodes and edges of the sample (Fig. 3C-D). Analysis of the processed digital structures suggested that the branch length distribution was best described by the half-normal distribution (Fig. 3E and Tabs. S1 and S2). The longest branch detected did not exceed 100 $\mu$m, and the tail of the branch length distribution was characterized by a relatively high shape parameter of the powerlaw distribution ($\mu = 7.65$, Fig. 3F)[23]. Importantly, sinusoids tend to branch at a small angle which is likely to improve blood flow (Fig. 3G)[24]. Finally, analysis of the neighboring nodes in the network (Fig. 3D) suggests that sinusoids connecting two adjacent nodes tend to be straight (Fig. 3H). Taken together, it seems remarkable how properties of the liver sinusoids such as small branching angles, straightness, and shortness match the observed pattern of movement of liver-localized T cells (e.g., Fig. 2F and Fig. 3F).

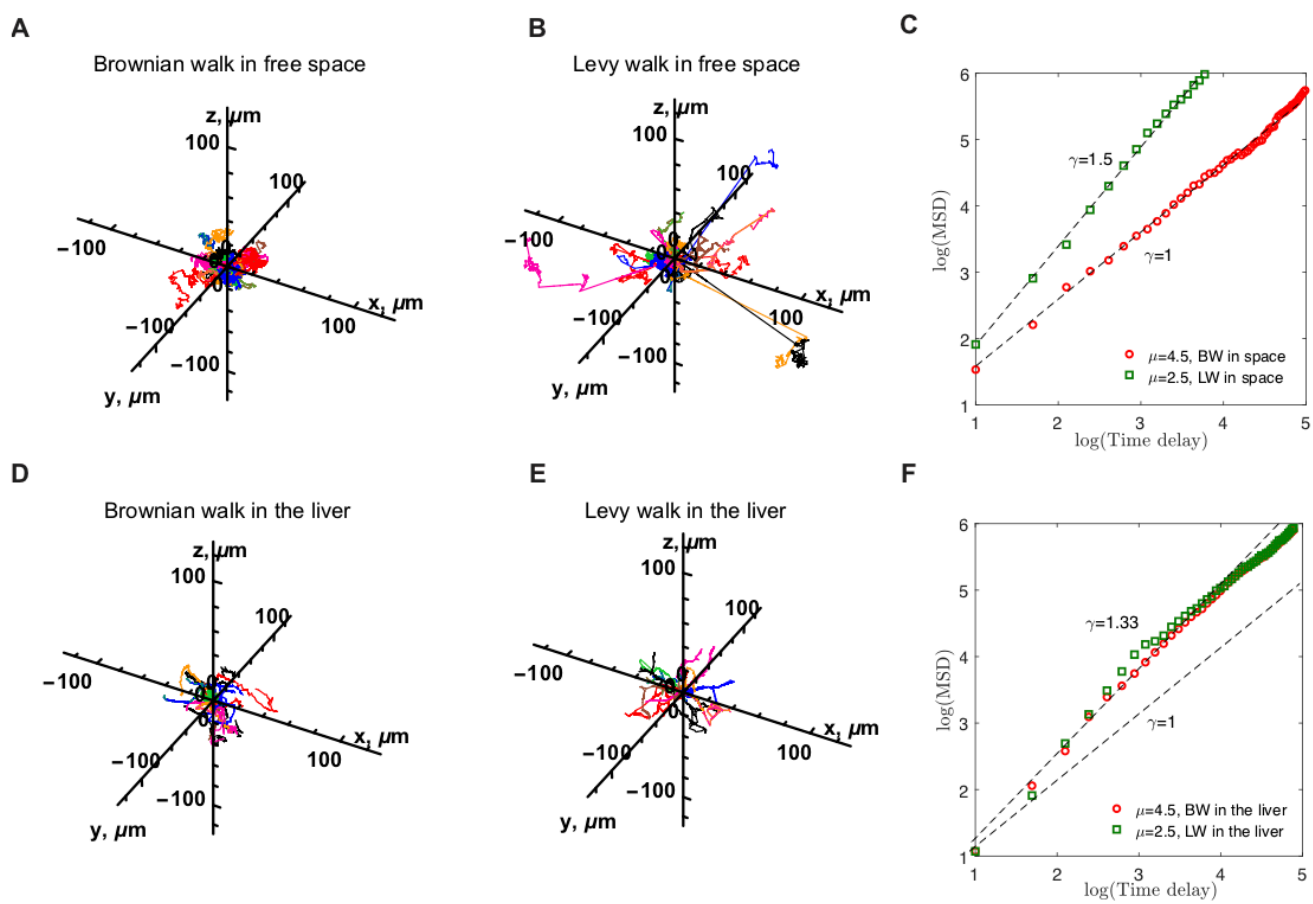


**Figure 4:** Liver structure imposes strong constraints on the movement pattern and overall displacement for Brownian or Levy walkers. We simulated movement of 200 T cells assuming that their movement length distribution is described by Pareto (powerlaw) distribution (see eqn. (S.9)) with $\mu = 4.5$ (i.e., Brownian walkers, A&D) or $\mu = 2.5$ (i.e., Levy walkers, B&E). T cells moved in free environment with no constraints (A-C) or are constrained by liver sinusoids (D-F). A sample of 20 cell trajectories is shown in A-B & D-E. (C)&(F). We calculated the MSD for the walkers and estimated the displacement slope $\gamma$ by linear regression of the initially linear part of the ln-transformed data. In free space simulations turning angle distribution for moving T cells was generated using uniform spherical distribution, while in liver sinusoids movement was set forward along the sinusoidal mean path. The average movement length per time step was $\bar{r} = 2.1$ $\mu$m as in our data with time step of 26 sec. An example of a simulated T cell movement in the liver is shown in Fig. S5 (see Materials and Methods for more details).

To investigate how the structure of the liver sinusoids may impact the movement patterns of cells with an intrinsic movement program we simulated movement of cells assuming that they are

either Brownian or Levy walkers with the preference of forward movement (Fig. 4). We assumed that distribution of movement lengths follows a powerlaw distribution with the shape parameter $\mu$ being different between Brownian ($\mu = 4.5$) and Levy ($\mu = 2.5$) walkers[22]. As expected in free 3D space Brownian walkers displayed normal diffusion ($\gamma = 1$) while Levy walkers superdiffused ($\gamma = 1.5$, Fig. 4A-C). In contrast, when cells were run on the digitized network of liver sinusoids (Fig. 3A-D) with cells allowed to make a random choice of turning when reaching a branching point the movement pattern changed dramatically (compared Fig. 4A vs. D and B vs. E). Impressively, both Brownian and Levy walkers displayed superdiffusion in the liver structure for substantial period of time ($\sim 55$ time steps, Fig. 4F) with the diffusion becoming normal at longer time scales. This pattern is similar to small particles displaying transient superdiffusion early and normal diffusion later due to motion of self-propelling bacteria in media[25]. Thus, the structure of the liver sinusoids seems to be sufficient to allow superdiffusion of Brownian walkers such as crawling liver-localized CD8 T cells.

It is surprising that structure of liver sinusoids was sufficient to allow Brownian walkers to superdiffuse without the need for chemical cues in the environment (e.g., chemokines). Because previous studies have suggested that T cells in lymph nodes (LNs) are close to Brownian walkers[11] we sought to determine if this is because of the structural constraints of the LN environment. It has been suggested that T cells use the network of fibroblastic reticular cells (FRCs) or dendritic cells (DCs) as a guide for movement[26,27]. Recently, the FRC network of the LNs has been imaged using confocal microscopy[28]. Using a similar computational pipeline we digitized the FRC network using previously published data[28] and calculated its basic characteristics (Fig. S6A-C). Interestingly, similarly to liver sinusoids the FRC network had relatively short branch lengths with tail of the distribution well described by the powerlaw distribution with a shape parameter $\mu = 6.7$ (Fig. S6D). A half-normal distribution fitted the data on branch length distribution with best quality (Fig. S6E and Tabs. S1 and S2). Similarly to the liver sinusoids FRC network has relatively small branching angles at the nodes, and connections between adjacent nodes are mostly straight (Fig. S6F-G). By assuming that T cells can only walk in the middle of the digitized FRC networks with preferred movement forward simulations of T cell walks suggested that independently whether cells do Brownian ($\mu = 4.5$) or Levy ($\mu = 2.5$) walks they display superdiffusion (Fig. S6H). However, analysis of the experimental data on movement of naive CD8 T cells in murine LNs[28] suggested that such T cells are not superdiffusive (Fig. S7). The duration of a persistent walk of T cells in LNs is around 4-5 min while CD8 T cells in the liver superdiffuse for nearly 20 min (Fig. S8). Analysis of the actual moving tracks of T cells in LNs suggests that many T cells tend to turn after a short directed movement (Fig. S7A&E). Indeed, it is well known that naive T cells in LNs tend to be restricted to the T cell areas, most likely by the gradient of chemokines. In contrast, in the liver in the absence of specific infection liver-localized T cells are likely to be unconstrained in movement by chemokines but are constrained by the physical structure of the sinusoids. Our results, thus, suggest that while structural constraints of the liver or FRC network in LNs may allow for superdiffusion of T cells other factors such as attraction cues may impair cell's ability to superdiffuse.

One of the advantages of Levy walks as often cited is a high efficiency at locating rare targets[1,3,21]. However, evaluation of search efficiency is often done in free space ignoring physical constraints or pathways agents may encounter when searching for targets. We simulated the search for a single *Plasmodium* parasite by a liver-localized CD8 T cell assuming that the parasite induces no attraction to the infection site. When a CD8 T cell searches for the parasite in constraint-free space, Levy walkers require less time ($\bar{T}$) to locate the target (Fig. 5A&C) which is consistent with previous results[1,3]. Interestingly, when the search is performed in the digitized liver structures, Brownian walkers are on average more efficient at finding targets than Levy walkers (Fig. 5B&D) with smaller variance in the time to target. Furthermore, in 55% of simulations Levy walkers would take longer

than the slowest Brownian walker to find the target (Fig. 5D). This may be particularly important in the case of malaria where a failure to find all the targets in the liver within a fixed time period (e.g., 48 hours) will result in blood stage infection and fulminant disease.

The dramatic difference in search efficiency between Levy and Brownian walkers in free 3D space and in the liver is due to differences in the paths to the target. In the digitized liver there are essentially few short pathways between a T cell and the target, and Brownian walkers make consistently small movements moving closer to the target. In contrast, Levy walkers spend long periods of time pausing before performing a long run sometimes resulting in them reaching the target rapidly. However, long pauses also result in much longer overall time to the target, which increases the average search time substantially. Thus, our results suggest that as in the tale of "The Tortoise and the Hare" in the liver slow and steady Brownian walkers reach the target on average faster than irregular but rapid Levy walkers. Interestingly, however advantage of Brownian walks in the liver disappears when many T cells search for a single target (Fig. S9).

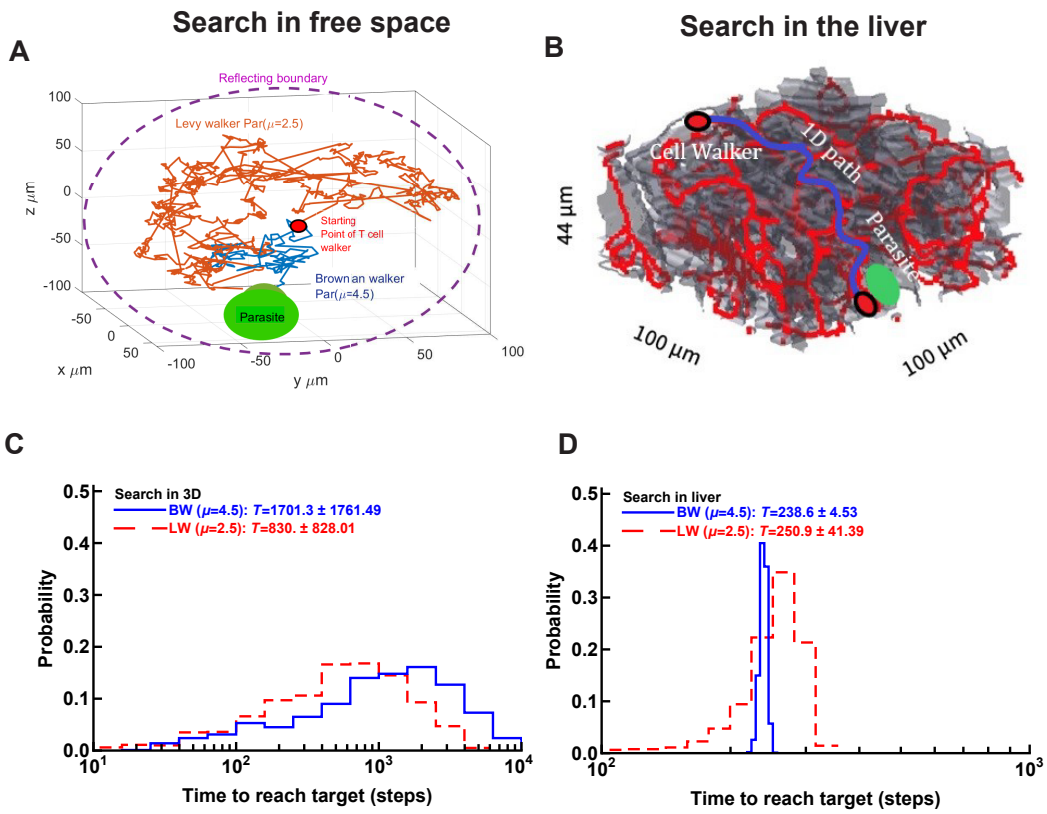


**Figure 5:** Levy walkers are less efficient in search for a single target in constrained environment of the liver. We simulated search of a T cell for a single target assuming Brownian (BW, $\mu = 4.5$) or Levy (LW, $\mu = 2.5$) walks in free space (A&C) or in liver sinusoids (B&D) and calculated the time it took for the T cell to locate the target (C&D). We assume that search occurs randomly (no attraction of the T cell to the target). (A)&(C) Levy walkers are more efficient in free space. We show distribution of times to the target for simulations when T cell started the search 100 $\mu$m away from the target. (B)&(D) Brownian walkers are more efficient in the liver. We show distribution of times to the target for simulations when T cell started the search 500 $\mu$m away from the target (mean $\bar{T}$ and standard deviation $\pm\sigma$ of the time is shown in C&D). In all simulations T cell was assumed to find the target when it was within 40 $\mu$m from the parasite (an approximate size of the murine hepatocyte). We simulated 1000 cells (3D) or 3000 cells (liver) under each scenario with average movement length per time step being $\bar{r} = 2.1$ $\mu$m in Pareto (powerlaw) distribution with the shape parameter $\mu$ (eqn. (S.9)).

# Discussion

T cells of the adaptive immune system are very efficient at locating and eliminating pathogens. However, the search strategies used by such efficient T cells remains poorly defined. It has been suggested that generalized Levy walks may be an evolutionary-selected cell-intrinsic strategy that allows brain-resident activated CD8 T cells to efficiently locate and eliminate *Toxoplasma gondii*-infected cells[3]. By analyzing novel data on movement of liver-localized CD8 T cells and linking these movement patterns to the digitized structure of liver sinusoids we showed that superdiffusion of T cells, the hallmark of Levy walks, may occur transiently in the absence of long range displacements. Such transient superdiffusion naturally arises due to the physical constraints imposed by narrow branching liver sinusoids instructing forward movement-biased T cells to move in a persistent direction with small turning angles. Interestingly, activated CD8 T cells may perform Levy flights in the liver in situations when they are poorly attaching to endothelial wall of the sinusoids and floating with the blood flow, thus, creating an impression of a long range movement[19,22]. Our results strongly suggest that observed pattern of superdiffusion or rare long range movements need not arise from cell-intrinsic movement programs but can be explained by the physical properties of the environment in which T cells move and preference of T cells to move forward. Importantly, we found that the widely cited advantages of Levy walks in searching for rare targets disappear if the search is done by a single T cell in biologically defined liver structures which effectively reduces target search problem from 3D to 1D.

Physical structures are unlikely to be the only constraint impacting the properties of T cell movements in tissues. We showed that FRC network of the lymph nodes (LNs) also allows for superdiffusion of agents in simulations; however, actual T cells in LNs do not superdiffuse (Figs. S7 and S8). Thus, other factors such as chemical cues (chemokines), finer details of the physical paths on which T cells walk such as FRCs/DCs, infection-induced inflammation, and preference of moving forward in the absence of external disturbances are likely to be also important in determining overall pattern of T movement in tissues. In particular, the role of environmental cues in determining agent movement patterns has been suggested in several systems[11,13].

Our results are likely to have broad implications for other systems in which superdiffusion and rare long range displacements have been observed or suspected[21,29]. It will be important to re-examine the evidence supporting intrinsic search programs by matching movement patterns of agents to the environmental details (e.g., airflows for albatrosses or currents for marine predators) and evaluating the role of cues (chemical or otherwise) in defining overall movement patterns of agents. Ultimately, future studies will need to quantify the relative contribution of intrinsic programs, environmental physical constraints, and cues in determining movement pattern of agents.

Our study has several limitations. Only a small area of the liver (approximately $500 \times 500 \times 50$ $\mu$m) is generally imaged with intravital microscopy which restricts the number of cells recorded and creates a bias for retention of slowly moving cells in longer movies. While we show that the digitized structure of liver sinusoids can override the intrinsic movement program of agents, we did not estimate how much of the experimentally observed movement pattern of liver-localized T cells is due to a cell-intrinsic program such as rare ability of cells to turn back, physical constraints of the liver sinusoids, or other environmental cues. Methods for discriminating between these alternatives will have to be developed. Finally, we have focused on explaining our data with simplest possible movement models involving movement length distribution, MSD, and turning angles. Other, more complicated Levy walk models have been suggested such as generalized Levy walks (GLW) or Zigzag-GLW which allow for runs and pauses and assume or generate heterogeneity in cell velocities[3,20,30]. However, such

models in general have more parameters, and fitting GLW-like models to data results in overfitting (results not shown). Our results, nevertheless, suggest that future studies focusing on benefits or evolutionary optimality of Levy walks would gain from more thorough investigation of the structural constraints and environmental cues that may be responsible for Levy-like observed movement pattern.

# Ethics statement

All animal procedures were approved by the Animal Experimentation Ethics Committee of the Australian National University (Protocol numbers: A2016/17; 2019/36). All research involving animals was conducted in accordance with the National Health and Medical Research Council's Australian Code for the Care and Use of Animals for Scientific Purposes and the Australian Capital Territory Animal Welfare Act 1992.

# Author contributions

VVG had the original idea for the study. VVG, HR, IAC, and JOC worked on various details of the experiments and analyses to be performed. JOC performed experiments (under supervision of IAC) and provided digitized data on movement of CD8 T cells in labeled liver sinusoids and separately provided images of labeled sinusoids. HR performed data curations, developed methods to digitize liver sinusoids and FRC networks and to analyze track data for T cells in the liver and LNs, ran most of data analyses and simulations, and wrote summaries of the methods and results. VVG wrote the first draft of the paper. All authors participated in the discussion of interim analyses and results. All authors contributed to the writing of the final version of the paper via changes, comments, and suggestions.

# Data sources

T cell movement/track data generated in this paper or in our previous publication are provided as an Excel spreadsheet with different tabs for different datasets. Imaging data of liver sinusoids (TIFF images) are also provided. The data from a previous publication on movement pattern of naive CD8 T cells in murine lymph nodes and imaging data of FRC networks in the LNs[28] are also provided. These files are stored together with the Matlab codes used to process and analyze the data on Github.

# Code sources

All analyses have been primarily performed in Matlab (ver 2019b) and codes used to generate most of figures in the paper are provided on GitHub: `https://github.com/vganusov/Levy_walks_liver.git`. All code questions should be addressed to H.R. (hanrajakaruna@gmail.com).

# Acknowledgments

We would like to thank Viktor Zenkov to contributing to the start of this work by manually digitizing liver sinusoidal maps and Marco Novkovic for providing imaging data of lymph nodes and data on movements of naive CD8 T cells in murine lymph nodes. This work was supported by the NIH grant (R01 GM118553) to VVG.

# Methods summary

To generate liver-localized CD8 T cells we followed our previously established protocol[19]. In short, naive TCR-transgenic OT-I cells, specific to an epitope from *Plasmodium* berghei (Pb-CS$^{5M}$) were stimulated *in vitro* with specific peptide (SIINFEKL) in the presence of IL-2. Four days after the culture, $5 \times 10^6$ cells were transferred into individual mice via tail vein, and prepared for liver imaging 2-4h after the injection (Fig. 1A). It takes few hours hours for activated CD8 T cells to attach and retain in the liver[19]. To label liver sinusoids we injected rhodamine-dextran i.v. 5-15 min prior to imaging (to allow for mouse preparation for liver imaging). Z-stacked images were processed using Imaris (Bitplane) to provide 3D coordinates of digitized cells over time. Imaging area was approximately $500 \times 500 \times 50$ $\mu$m. Cell positions were curated to make sure that measurements were done in consistent time intervals of 13 or 26 sec. For liver structure analysis another set of experiments involved injection of rhodamine-dextran or Evans blue 5-15 min prior to imaging (2 mice). Imaging was done using two photon microscope. Analyses of the imaging data or of cell coordinate data were done in Matlab or Mathematica (see extended description of the methods in Extended Methods online). T cell coordinate data and liver sinusoids imaging data are available on Github (see above).

# References

1. Viswanathan, G. M. *et al.* Optimizing the success of random searches. *Nature* **401**, 911–914 (1999). URL `http://dx.doi.org/10.1038/44831`.

2. Bartumeus, F., Catalan, J., Fulco, U. L., Lyra, M. L. & Viswanathan, G. M. Optimizing the encounter rate in biological interactions: Lévy versus Brownian strategies. *Phys Rev Lett* **88**, 097901 (2002).

3. Harris, T. H. *et al.* Generalized Lévy walks and the role of chemokines in migration of effector CD8+ T cells. *Nature* **486**, 545–548 (2012). URL `http://dx.doi.org/10.1038/nature11098`.

4. Edwards, A. M. *et al.* Revisiting Lévy flight search patterns of wandering albatrosses, bumblebees and deer. *Nature* **449**, 1044–1048 (2007). URL `http://dx.doi.org/10.1038/nature06199`.

5. Reynolds, A. M. Current status and future directions of Lévy walk research. *Biology open* **7** (2018).

6. Bartumeus, F. Levy processes in animal movement: an evolutionary hypothesis. *Fractals* **15**, 151–162 (2007).

7. Wosniack, M. E., Santos, M. C., Raposo, E. P., Viswanathan, G. M. & da Luz, M. G. E. The evolutionary origins of Lévy walk foraging. *PLoS computational biology* **13**, e1005774 (2017).

8. Reynolds, A. Liberating Lévy walk research from the shackles of optimal foraging. *Physics of life reviews* **14**, 59–83 (2015).

9. Miller, M., Wei, S., Parker, I. & Cahalan, M. Two-photon imaging of lymphocyte motility and antigen response in intact lymph node. *Science* **296**, 1869–73 (2002).

10. Banigan, E. J., Harris, T. H., Christian, D. A., Hunter, C. A. & Liu, A. J. Heterogeneous CD8+ T cell migration in the lymph node in the absence of inflammation revealed by quantitative migration analysis. *PLoS Comput Biol* **11**, e1004058 (2015). URL `http://dx.doi.org/10.1371/journal.pcbi.1004058`.

11. Krummel, M. F., Bartumeus, F. & Gérard, A. T cell migration, search strategies and mechanisms. *Nature reviews. Immunology* **16**, 193–201 (2016).

12. Ariotti, S. *et al.* Tissue-resident memory CD8+ T cells continuously patrol skin epithelia to quickly recognize local antigen. *Proc Natl Acad Sci U S A* **109**, 19739–19744 (2012).

13. Mrass, P. *et al.* ROCK regulates the intermittent mode of interstitial T cell migration in inflamed lungs. *Nature communications* **8**, 1010 (2017).

14. Ménard, R. *et al.* Looking under the skin: the first steps in malarial infection and immunity. *Nat Rev Microbiol* **11**, 701–712 (2013). URL `http://dx.doi.org/10.1038/nrmicro3111`.

15. Aleshnick, M., Ganusov, V. V., Nasir, G., Yenokyan, G. & Sinnis, P. Experimental determination of the force of malaria infection reveals a non-linear relationship to mosquito sporozoite loads. *PLoS pathogens* **16**, e1008181 (2020).

16. Schmidt, N. W. *et al.* Memory CD8 T cell responses exceeding a large but definable threshold provide long-term immunity to malaria. *Proc Natl Acad Sci U S A* **105**, 14017–22 (2008).

17. Krzych, U., Dalai, S., Zarling, S. & Pichugin, A. Memory CD8 T cells specific for plasmodia liver-stage antigens maintain protracted protection against malaria. *Front Immunol* **3**, 370 (2012). URL `http://dx.doi.org/10.3389/fimmu.2012.00370`.

18. Fernandez-Ruiz, D. *et al.* Liver-resident memory CD8(+) T cells form a front-line defense against malaria liver-stage infection. *Immunity* **45**, 889–902 (2016).

19. McNamara, H. A. *et al.* Up-regulation of LFA-1 allows liver-resident memory T cells to patrol and remain in the hepatic sinusoids. *Science Immunology* 1–10 (2017).

20. Zumofen & Klafter. Laminar-localized-phase coexistence in dynamical systems. *Physical review. E, Statistical physics, plasmas, fluids, and related interdisciplinary topics* **51**, 1818–1821 (1995).

21. Viswanathan, G., Raposo, E. & Da Luz, M. Lévy flights and superdiffusion in the context of biological encounters and random searches. *Physics of Life Reviews* **5**, 133–150 (2008).

22. Zaburdaev, V., Denisov, S. & Klafter, J. Lévy walks. *Rev. Mod. Phys.* **87**, 483–530 (2015). URL `https://link.aps.org/doi/10.1103/RevModPhys.87.483`.

23. Clauset, A., Shalizi, C. R. & Newman, M. E. J. Power-law distributions in empirical data. *SIAM Rev.* **51**, 661–703 (2009). URL `http://dx.doi.org/10.1137/070710111`.

24. Murray, C. D. The physiological principle of minimum work applied to the angle of branching of arteries. *The Journal of general physiology* **9**, 835–841 (1926).

25. Kanazawa, K., Sano, T. G., Cairoli, A. & Baule, A. Loopy lévy flights enhance tracer diffusion in active suspensions. *Nature* **579**, 364–367 (2020).

26. Bajénoff, M. *et al.* Stromal cell networks regulate lymphocyte entry, migration, and territoriality in lymph nodes. *Immunity* **25**, 989–1001 (2006).

27. Krishnamurty, A. T. & Turley, S. J. Lymph node stromal cells: cartographers of the immune system. *Nature immunology* **21**, 369–380 (2020).

28. Novkovic, M. *et al.* Topological small-world organization of the fibroblastic reticular cell network determines lymph node functionality. *PLoS biology* **14**, e1002515 (2016).

29. Wosniack, M. E., Santos, M. C., Raposo, E. P., Viswanathan, G. M. & da Luz, M. G. E. Robustness of optimal random searches in fragmented environments. *Physical review. E, Statistical, nonlinear, and soft matter physics* **91**, 052119 (2015).

30. Li, H. *et al.* Zigzag generalized lévy walk: the in vivo search strategy of immunocytes. *Theranostics* **5**, 1275–1290 (2015).

31. Ta-Chih Lee, R. L. K. & Chu, C.-N. Building skeleton models via 3-D medial surface/axis thinning algorithms. *Computer Vision, Graphics, and Image Processing* **56**, 462–478 (1994).

32. Kollmannsberger, P., andFelix Repp, M. K., Wagermaier, W., Weinkamer, R. & Fratzl, P. The small world of osteocytes: connectomics of the lacuno-canalicular network in bone. *New Journal of Physics* **19**, 073019 (2017).

33. Newton, I. *Newton's Principia: the mathematical principles of natural philosophy* (New York: Daniel Adee).

34. Cockburn, I. A. *et al.* In vivo imaging of CD8+ T cell-mediated elimination of malaria liver stages. *Proc Natl Acad Sci U S A* **110**, 9090–9095 (2013). URL `http://dx.doi.org/10.1073/pnas.1303858110`.

35. Kelemen, R. K., Rajakaruna, H., Cockburn, I. A. & Ganusov, V. V. Clustering of activated CD8 T cells around malaria-infected hepatocytes is rapid and is driven by antigen-specific cells. *Frontiers in immunology* **10**, 2153 (2019). URL `Bioaxiv: doi:10.1101/508796.`

36. Cockburn, I. A., Tse, S.-W. & Zavala, F. CD8+ T cells eliminate liver-stage Plasmodium berghei parasites without detectable bystander effect. *Infect Immun* **82**, 1460–1464 (2014). URL `http://dx.doi.org/10.1128/IAI.01500-13`.

37. Zenkov, V. S., O'Connor, J., Cockburn, I. A. & Ganusov, V. V. A minority of liver-localized CD8 T cells demonstrate difficult-to-detect attraction to Plasmodium-infected hepatocytes. *bioRxiv* (2020). URL `https://doi.org/10.1101/2020.12.12.422451`.

# Supplemental Information

Environment-imposed constraints can make Brownian walkers efficient searchers

Harshana Rajakaruna, James O'Connor, Ian A. Cockburn, Vitaly V. Ganusov

# Materials and Methods

## Experimental Details

**T cell movement in the liver**. Experimental data on movement of wild type (WT), GFP-expressing, TCR transgenic CD8 T cells (OT-I) have been generated similarly as in our previous study[19]. OT-I cells were activated *in vitro* as follows. Splenocytes were incubated with 1 $\mu$g/ml SIINFEKL peptide (Biomatik) at 37$^{o}$C for 30 minutes, washed, and cultured in complete RPMI 1640 (10% FCS, 2mm L-glutamine, 1mm Na-Pyruvate, 100U/ml Penicillin/Streptomicin, 5mm HEPES, 20 $\mu$g/ml Gentimicin and 50 $\mu$M $\beta$-mercaptoethanol) at 37$^{0}$ C, 5% $CO_2$. Two days later cells were passaged and cultured in fresh media supplemented with (12.5U/ml) recombinant IL-2 (PeproTech). Cells were passaged again after 24 hours, and given fresh media with IL-2. Four days after activation cells were ready for collection and use. Cells were collected from tissue culture flasks, washed, layered over Histopaque® 1083 (Sigma) and centrifuged at 400rcf, for 30 minutes at 21$^{0}$C to remove dead cells. Live lymphocytes were collected from the interface between the Histopaque® and cell suspension media. Cells were washed a further 3 times prior to transfer to mice.

To label the sinusoids, Evans blue or Rhodamine-dextran were injected i.v. into mice (50 $\mu$g/mouse) immediately prior to imaging of the livers (Fig. 1A&B). In some cases, static images of the livers were acquired using two phone microscope. In total, we have generated images of the liver sinusoids from 5 mice (with or without T cells).

Mice were prepared for multi-photon microscopy essentially as previously described[19]. Briefly, mice were anesthetized with a mix of Ketamine (100 mg/kg) and Xylazine (10 mg/kg). Throughout the surgery and imaging procedure the mouse temperature was maintained at 37$^{o}$C using a heating mat attached to feedback probe inserted in the mouse rectum. A lateral incision was made over the left lobe of the liver and any vessels cauterized by applying light pressure to the vessel until clotting occurred naturally. The mouse was then placed in a custom made holder. The liver was then exposed and directly adhered to a coverslip that was secured in the holder. Once stable the preparation was transferred to a Fluoview FVMPE-RS multiphoton microscope system (Olympus) equipped with a XLPLN25XWMP2 objective (25x; NA1.05; water immersion; 2mm working distance). For analysis of the motility of liver-localized CD8 T cells a 50 $\mu$m z-stack (2 $\mu$m/ slice) was typically acquired using a standard galvano-scanner at a frame rate of 2-4 frames per minute.

Other datasets for movement of WT and LFA-1-deficient CD8 T cells, or WT CD8 T cells 1 or 4 weeks after immunization with radiation-attenuated *Plasmodium berghei* sporozoites Pb-CS$^{5M}$ were generated previously[19].

**Imaging data processing and basic analyses**. Raw imaging data was analyzed with Imaris x64 software (Bitplane) v9.12. Tracking of individual cells in a z-stack was performed using the 'Spots' function in the surpass mode, and in a single slice by the 'Surfaces' function in surpass mode. Detection of individual cells relied upon their relative fluorescence intensity, size (diameter $\geq$ 9 $\mu$m) and used the remaining default function settings for the calculation of the motion tracks

using an autoregressive motion algorithm. Basic cell characteristics such as average track speed, meandering index and arrest coefficient were calculated using Imaris. To calculate the percentage of T-cell movements that were occurring in the sinusoids we generated a co-localization channel which calculated colocalized signal of both red and green fluorescence within each frame. To do this, we utilised the colocalization function on Imaris with the threshold defined in Imaris as 16 for uGFP OT-1 cells which subtracted background fluorescence of the liver, and 3000 for rhodamine dextran. We then calculated the total number of frames a T-cell was tracked using the unique cell ID, and compared this to the total frames each individual T-cell was detected in the designed colocalization channel. Rhodamine dextran fluorescence was dependent on the depth of imaging, and in the lower Z-stacks the frequency of T-cells with colocalized signal was poor (results not shown).

**Data details and data cleaning steps**. In our analysis we used 3D coordinates of Plasmodium-specific CD8 T cells in the liver over time from the following experiments:

1. Novel data on movement of GFP-expressing activated CD8 T cells called "New13" and "New26". In the "New13" dataset data were generated from three mice and frames were sampled at 14.63 (14.63-14.64) sec apart. In the "New26" dataset data were generated from two mice, and frames were sampled on average at 25 (24.29, 25.51) sec apart. To increase the power in the analysis we generated a combined dataset "New1326" by merging data from datasets "New13" and "New26". We ignored the mid time-points in time-frames in the "New13" dataset, thus, computing time-frames approximately at 26 sec frequency.

2. Previously published data on movement of WT and LFA1-deficient CD8 T cells in the liver[19] resulted in "Lfa1 WT" and "Lfa1 KO" datasets. Data were from 7 mice, and frames were sampled, on average, at 27 (24.65 - 29.56) sec apart.

3. Previously published data on movement of *Plasmodium*-specific CD8 T cells following vaccination of mice with radiation-attenuated sporozoites[19]. In "Wk1" dataset data were generated from two mice immunized with RAS 1 week before. Frames were sampled, on average, at 6.51 (6.51-6.51) sec apart. In "Wk4" dataset five mice were RAS-immunized 4 weeks prior to imaging, and frames were sampled, on average, at 3.25 (3.25-3.26) sec.

4. Novel data on movement of *Plasmodium*-specific (OT-1) and lymphocytic choriomeningitis virus-specific (P14) CD8 T cells moving in livers of *Plasmodium berghei*-infected mice (Zenkov et al. Bioarxiv link).

In the Imaris-processed movies we found that there were random missing time-frames in tracks in nearly all data. This could happen when Imaris would associate a cell that went out of focus for one time step with other time steps. Because having a consistent time step to determine cell movement characteristics such as mean squared displacement and movement length distribution was critical we cleaned the data in the following ways. We split tracks with missing time frames and converted them to individual cells for the analyses. For example, if one time frame was missing for a cell, the track was split into two with the second part being assigned as a new "cell". This created many more cells with shorter tracks. Taken together, cleaning up the data yielded the following. For "New13" dataset we originally had 56 T cells out of which we generated 14 new split cells with 1-2 splits resulting in total of 70 T cells with 2565 time-frames (movements). For "New26" dataset we had 213 T cells with 51 new split cells with 1-2 splits from the original tracks totaling to 264 T cells, with 7736 time-frames. For the combined "New1326" dataset we had 334 T cells with 9018 time-frames. For "Lfa1 WT" dataset we originally had 198 T cells out of which we generated 19 new

split cells with 1-2 splits from the original tracks totaling to 217 T cells, with 6210 time-frames. For "Lfa1 KO" dataset we originally had 154 T cells out of which we generated 16 new split cells with 1-2 splits from the original tracks totaling to 170 T cells, with 5097 time-frames. For "Wk1" dataset we had 99 T cells and generated 3 new split cells with 1-2 splits from the original tracks, totaling to 102 T cells, with 2525 time-frames. For "Wk4" dataset we had 44 T cells with 4169 time-frames that required no cleaning. Most of the analyses have been repeated on "clean" data in which tracks with missing time-frames were removed with similar conclusions reached.

**T cell movement in the LNs**. Data have been provided by Mario Novkovic from their previous publication[28]. In short, $3 \times 10^6$ naive P14 TCR transgenic T cells were transferred i.v. into naive mice. Three to twenty-four hours after T cell injection, intravital imaging was performed on the right popliteal LNs. To detect FRCs, anti-YFP mAbs were used and samples were imaged using a confocal microscope (LSM-710; Carl Zeiss)[28]. In total we had 3 sets of images of LNs with FRCs labeled (about 30 images per set with 2 µm depth). In addition, we analyzed 3D movement data of T cells in the LNs (in total 6 movies) produced in the same publication[28]. The data were also cleaned and tracks for which there were not always consecutive timeframes available were split as described above. Analyses were repeated with "clean" data in which cells with missing time-frames were removed; similar results were found. These data were generated at frequency of 20 sec per frame.

## Modeling and Statistical Analytical Methods

**Mean squared displacement, turning angles, and velocity correlations**. For each of the datasets we calculated several basic characteristics. To calculate mean squared displacement (MSD) we used all tracks in the dataset in which time frequency of measurements was approximately the same:

$$\mathrm{MSD}(t) = \frac{1}{N(t)} \sum_{i=1}^{N(t)} r_{i,t}^2, \tag{S.1}$$

where $r_{i,t}$ is the displacement of an $i^{th}$ cell from its initial position to the position at time $t$ and $N(t)$ is the number of cells for which coordinate data were available at time $t$. To characterize the MSD we used the following relation $\mathrm{MSD}(t) = ct^\gamma$ where $t$ are lag-times or delays, and $\gamma$ was estimated by log-log transforming MSD and $t$. Estimate of $\gamma < 1$ suggests subdiffusion of cells, whose walks are constrained by boundaries, regardless of their step length distribution, $\gamma = 1$ suggests Brownian (or normal) diffusion, whose walks are affected by neither boundaries nor transportation, whereas, $\gamma > 1$ suggests superdiffusion, whose walks are indicative of transportation or directed movements. Root mean squared displacement, $\zeta = \mathrm{RMSD}$ was calculated as

$$\zeta(t) = \mathrm{RMSD}(t) = \sqrt{\mathrm{MSD}}, \tag{S.2}$$

where MSD is defined in eqn. (S.1). To calculate turning angle for cell movement between time steps $(t, t+1)$ and $(t+1, t+2)$ we calculated the vectors of movements between two time points and then calculated the angle between these two movement vectors. To estimate decay in the correlation movements of a T cell over time we calculated the vector for the initial T cell velocity $\bar{v}_1$ (movement vector for a cell from $t = 0$ to $t = 1$), vector for later movement $\bar{v}_t$ (movement vector for a cell between times $t-1$ and $t$), and the angle $\phi_{1,t}$ between the two vectors $\bar{v}_1$ and $\bar{v}_t$:

$$c_V = \cos(\phi_{1,t}), \tag{S.3}$$

where by definition $c_V$ varies between -1 and 1.

**Basic statistical distributions to describe movement length data**. To investigate which model is best consistent with the distribution of movement/step lengths of activated CD8 T cells in the liver or distribution of branch lengths of liver sinusoids we fit several alternative distributions to the data. Cauchy distribution is defined as

$$f(r|\gamma) = \frac{1}{\pi\gamma}\left[\frac{\gamma^2}{\gamma^2 + (r - r_{\min})^2}\right], \tag{S.4}$$

where $r \geq r_{\min}$ is the displacement, $r_{\min}$ is the location parameters, and the mean of the distribution is undefined. Half-gaussian distribution with $r \geq 0$ is defined as

$$f(r|\sigma) = \frac{\sqrt{2}}{\sqrt{\pi}\sigma}\mathrm{e}^{-\frac{r^2}{2\sigma^2}}, \tag{S.5}$$

where mean of the half-normal distribution is $\bar{r} = \sigma\sqrt{2/\pi}$.

Stable Levy (SL) distribution is defined as

$$f(r|\gamma) = \frac{\sqrt{\gamma}}{\sqrt{2\pi}(r - r_{\min})^{3/2}}\mathrm{e}^{-\frac{\gamma}{2(r-r_{\min})}}, \tag{S.6}$$

where $\gamma$ and $r_{\min}$ are the shape parameter and location parameter, respectively. The SL distribution has infinite mean and variance.

Generalized Pareto (GP) distribution is defined as

$$f(r|k, \sigma, \theta) = \frac{1}{\sigma}\left(1 + \frac{k(r - \theta)}{\sigma}\right)^{-1-\frac{1}{k}}, \tag{S.7}$$

where $k$ is the shape parameter, $\sigma$ is the scale parameter, and $\theta$ is the location parameter. In this distribution, the mean is $\bar{r} = \theta + \sigma/(1 - k)$.

When $k = 0$ and $\theta = 0$, GP becomes exponential distribution

$$f(r|\lambda) = \lambda\mathrm{e}^{-\lambda r}, \tag{S.8}$$

where $\lambda = 1/\sigma$, and mean being equal to $\bar{r} = \sigma$. When $k > 0$, $\theta \to 0$ GP becomes the Pareto (or Powerlaw) distribution

$$f(r|r_{\min}, \alpha) = \frac{\alpha r_{\min}^{\alpha}}{r^{\alpha+1}} = \frac{(\mu - 1)r_{\min}^{\mu-1}}{r^{\mu}}, \tag{S.9}$$

where $r_{\min} = \sigma/k$ (scale parameter), $\alpha = 1/k$, $\mu = \alpha + 1$ (shape parameter), and $\bar{r} = (\mu - 1)r_{\min}/\mu$. Note that in Pareto distribution $r \geq r_{\min}$. The important property of the Pareto distribution, describing either Brownian or Levy walks, is dependence of the mean and variance on the value of

$\mu$ (and thus $\alpha$). For $\mu > 3$ ($\alpha > 2$), both mean and variance of the Pareto distribution are finite corresponding to Brownian walk. In contrast, when $\mu \leq 3$ ($\alpha \leq 2$) mean is finite and variance is infinite corresponding to Levy walks. Finally, when $\mu \leq 2$ ($\alpha \leq 1$), both mean and variance are infinite corresponding to bullet motion[22].

Generalized extreme value (GeV) distribution is defined as

$$f(r|\mu, \sigma, \xi) = \frac{1}{\sigma} t(r)^{\xi+1} \mathrm{e}^{-t(r)}, \tag{S.10}$$

where $t(r) = \begin{cases} (1 + \xi \frac{(r-\mu)}{\sigma})^{-1/\xi}, & \text{if } \xi \neq 0, \\ \mathrm{e}^{-(r-\mu)/\sigma}, & \text{otherwise.} \end{cases}$

**Statistical methodology of fitting models to data**. We fit the models (eqns. (S.4)–(S.9)) to either actual displacements $r$ (movement lengths) or scaled displacements $\rho$. Scaled displacements are defined as $\rho = r(t)/\zeta(t)$, where $\zeta(t)$ was calculated over the time period $t$ (eqn. (S.2)). It is important to emphasize that scaled displacements $\rho$ allows to convert cell tracks to be independent of the effect of different mean speeds of individual cells and independent of the effect of different sampling frequency[3]. Likelihood of the model parameters given the data is given as

$$L(m_1, m_2, ...|x_1, x_2, ...., x_n) = \prod_{i=1}^{n} f(x_i|m_1, m_2, ...), \tag{S.11}$$

where $x_i$ are either the cell movement length data $x_i = r_i$ or the scaled displacement data $x_i = \rho_i(t) = r_i/\zeta_i(t)$, for $i = 1...n$, for $n$ data points, for fixed time intervals $t$. The probability density functions $f(x_i|m_1, m_2, ...)$ are given in eqns. (S.4)–(S.9). Parameters $m_1, m_2, ...$ of the models were estimated by minimizing the log of negative likelihood, $\mathcal{L} = -\ln L$.

**Tail analysis of the step length distribution**. In addition to fitting different distributions to the movement length/displacement data we performed an analysis to determine the shape parameter of the powerlaw/Pareto distribution $\mu$ that is best consistent with tail of the displacement distribution data[23]. Given that Pareto distribution has two parameters ($r_{\min}$ and $\mu$, eqn. (S.9)) one needs to define $r_{\min}$ that determine the cut-off in the data and that allows for the best description of the tail of the data with Pareto distribution. The steps to define $r_{\min}$ are as follows[23]: (1) for each possible choice of $r_{\min}$ from the smallest to the largest unique values of $r$, we computed $\mu$ by maximum likelihood estimate given by the analytic expression $\hat{\mu} = 1 + n \left( \sum_{i=1}^{n} \ln \frac{r_i}{r_{\min}} \right)^{-1}$, where $r_i$, $i = 1...n$, are the observed values of $r$ and $r_i \geq r_{\min}$. In doing so, we also set a limit to the number of data points in the analysis by setting a criteria by which the analysis is terminated if the standard error on $\hat{\mu}$, approximately given by $\sigma = \frac{\hat{\mu}-1}{\sqrt{n}}$, was greater than 0.1, as higher order corrections of the standard error are generally positive. This condition was set because the estimates of $\mu$ can be erroneously large when $r_{\min}$ is so large that the number of observed $r \geq r_{min}$ is very small. It was also assumed that $\mu > 1$, since the distributions with $\mu \leq 1$ are not normalizable, and hence not realistic in nature. We selected $r_{\min}$, at which the Kolmogorov-Smirnov (K-S) goodness-of-fit statistic $D$ was the minimum out of all $D$ values given by the fits over all possible unique $r_{\min}$'s of the data. Here, we also made a finite correction to the estimates of $\mu$ for small sample sizes ($n < 50$) in addition to the condition set by the standard error of $\mu$.

From the above analyses, we carried forward the estimated $r_{\min}$, $\mu$, and $D$ to the next stage of testing the probability of the data, given that the estimated model is the plausible one, by the method

of Kolmogorov-Smirnov goodness-of-fit test. To do that we generated data from the hypothesized (or estimated) Pareto model, sampling using a semi-parametric bootstrap method, computing $D$ for each sample, which is the synthetic $D$, and thus, computing a fraction of those were greater than the empirical $D$ of the given data, which yields the $p$ value of the hypothesis. We then computed the uncertainty in the estimates of $r_{\min}$, $\mu$, and $n$, given by standard deviations, by resampling the data with replacements by Markov chain Monte Carlo (MCMC) simulations.

**Digitizing and skeletonizing the 3D sinusoidal structure**. We analyzed 23 z-stacks of Evans blue stained $512 \times 512$ $\mu$m images of the liver (mouse 1: 171207 and mouse 2: 190624), as well as 3 sets of images/movies with T cells in which liver sinusoids were labeled with rhodamine-dextran. Resulting structures were similar based on calculated characteristics such as branching angle distribution and straightness index (results not shown). Light-adjusted 2D images were converted from RGB into grayscale using rgb2gray, filtered through Matlab filters (1) imfilter with Gaussian N(10,2) to remove noise, (2) medfilt2, with 'symmetric' setting to remove all the lines from the image, (3) uint8 to subtract image without lines from image with lines, (4) setting threshold at $> 130$ of the subtracted image, and (5) removing more noise by imopen, and saving all 2D images in a stack converting to a digitized 3D image, with "1" giving the sinusoids and "0" giving the hepatocytes and other unstained tissues (Fig. 3). The digitized 3D image was then skeletonized with 1's giving the mean path of sinusoids and 0's elsewhere, converting to a voxel image, using parallel medial axis thinning method as per the MATLAB vectorized implementation of the algorithm[31]. The 3D binary voxel skeleton was converted to a network graph, computing nodes (junctions) and edges (branches), using previously published methods[32], and mapping the respective skeleton to 3D graphics function. The nodes and the branches were used to compute branch angles, branch lengths, node-to-node direct distances, number of branches per node. Straightness of branches metric was computed as the node-to-node direct distance over the branch length. The binary 3D liver image was used to run simulations of cells walking on the 1's on the lattice, scale of which can be decided, for e.g., 1 unit equals 0.01 µm (Fig. 4).

**Simulation methods of cell walks on digitized sinusoidal structures and analyses of re-sampled step-length distribution and MSD**. We simulated cell walks on (i) digitized 3D real sinusoidal branch structures (5 imaging sets), (ii) simulated sinusoidal branch structures generated from both Levy-like (5 simulations) or truncated Pareto and Gaussian (5 simulations) branch length distributions, with branch angles generated from random (spherical uniform) and empirical distributions from real structural samples, and (iii) no structures (5 simulations) imposing no physical constraints giving freedom for cells to turn any direction after every step. For each generated structure we selected a random point on a mean sinusoidal path, i.e. on the digital skeleton given by 1's, on the matrices generated from digitized 3D sinusoidal structures of 1's and 0's in the real case, and on a branch position coordinate in the simulated case, as the starting point of a T cell. Then we selected a cell step-length from the following specified displacement distributions in unit time: (i) phenomenologically best-fitted truncated Generalized Extreme Value distribution with parameter $1 > \xi > 0.5$, i.e, heavy-tailed Levy-like with infinite variance, yet finite mean (eqn. (S.10)); (ii) half-Gaussian (eqn. (S.5)); (iii) Composite models with Pareto tails, approximating Levy and Gaussian tails, with Gamma heads (eqn. (S.9)), and (iv) Convoluted model (generalized Levy walks as described previously[3,30]), approximating Levy tails in (Pareto) runs and pauses, or observed and unobserved step-lengths), and walked the cell digitally along the sinusoidal path to the next point on the matrix, sampled the step-end coordinates at fixed time intervals. Note that we considered all movements as forward movements, as reverse movements of cells along the sinusoids were the minority in the data (about 20%, Fig. S2). Ability of cells to move in one preferred direction in constant external conditions can be viewed similarly to the physics postulate of

momentum conservation (or "biological inertia",[33]). We disregarded deviation of tracking cell centers from the mean sinusoidal path because the cell diameter, on average, 10 $\mu$m, was greater than the cylindrical diameter of the sinusoids, 7 $\mu$m, and thus, T cells likely occupied most of the cross-sectional area of the sinusoids. Note also that step-lengths and branch lengths were thus simulated disregarding their autocorrelations assuming they are independent and identically distributed (i.d.d.). Cell walk simulations on no-structure, the cell turning angles were random from a uniformly spherical distribution. Note that the walk simulations of cells and sampling coordinate were terminated once a cell hits the boundary of the structure before the simulation time was elapsed in the case of real sinusoidal structures.

We simulated cell walks on i) no structure (i.e., free 3D space), or ii) digitized 3D real sinusoidal structure. To simulate T cell walk in digitized liver sinusoids, we selected a random point on a mean sinusoidal path, i.e. on the digital skeleton given by 1's, on the matrices generated from digitized 3D sinusoidal structures of 1's and 0's. We selected step-lengths of the simulated walks from a Pareto distribution with $\mu = 2.5$ and $\mu = 4.5$ with the same mean (eqn. (S.9)), assuming Levy vs. Brownian walk scenarios, and motion of cells strictly forward along the sinusoid mean paths. We chose 200 cells with each walking 50 steps to match the average time observations of the real data within the limited 3 dimensions of the structure. Simulation with no structure we did the same and selected turning angles from a uniform spherical distribution. We computed MSD of all four scenarios. To simulate T cell walks in digitized 3D network of FDCs in LNs we proceeded similarly to the method for liver sinusoids assuming that T cells can only walk in the middle of the network path and turns can be taken only when a T cell reaches a branching point.

**Simulation methods of computing efficiency of cells finding a target**. We computed two metrics of efficiency of cells finding a target on the structure vs. no structure: (i) mean and variance of time-to-reach a random target (100 targets) on the walk path in a structure, given cells with two types of walk characteristics (at least 1,000 cells in each): powerlaw/Pareto with different values of the shape parameter $\mu$; using the same path on (a) Gaussian and truncated-Levy branch structures, with random and empirical branch angles; (b) real structures; and (c) no-structure with uniformly spherically distributed turning angles; (ii) mean and variance of time-to-hit a given random target (300 targets), given that they did not miss the target, for cells (10,000 for each), walking Gaussian vs truncated-Levy step-lengths, starting from a random point on the same structures vs. no-structure, given cell-absorbing structural boundaries in the structures, assuming cells absorbed missed the target; and (iii) the probability of a cell hitting the target, simulating walks as same as above. We repeated the simulation with 5 different distances to targets, taken geometrically, from the initial points, and also with multiple targets with different densities in space (results not shown). We started simulations at different distances between a T cell and the target and assumed that T cell found the infected cell when it was within 40 $\mu$m from the target, an approximate size of the murine hepatocyte[34,35]. For 3D simulations if searching T cell reached the boundary we assumed that it missed the target (and thus was not included in the calculation of the average time). For simulating T cells searching for a target in the liver we simulated T cells moving forward on one path, effectively reducing search problem to 1D. This is reasonable given that difference between Brownian and Levy walks is only on the movement length distributions and not on turning angles that cells take[22]. To simulate $n$ T cells searching for a single sample, assuming that search is done by different cells independently, we resampled times to target with replacement $n$ times from the dataset on a single T cell searching for a single target, and calculated minimal of the time in the sample. This procedure was them repeated 1,000 times to generate a distribution to target when $n$ T cells search for the infection site.

**Detailed characterization of the movement patterns of T cells**. In the main text we focused on characterizing movement patterns of CD8 T cells in the liver or the LNs by calculating MSD for cells and the distribution of movement lengths and comparing the latter data to several well-characterized parametric distributions. This is a standard approach to detect whether moving agents undergo Brownian or Levy walks[3,4]. However, several alternative movement types may result in similar (or identical) MSD and movement length distributions. Other characteristics such as RMSD, distribution of turning angles or T cell velocities may provide additional information that may explain specific patterns of cell movement[3,30]. Our finding that liver-localized CD8 T cells undergo only small movement steps is fully consistent with the Brownian walk; however, this does not prove that walks are indeed Brownian. We found that T cell movement program in which cells move as generalized Levy walkers with long but rare movements/runs ($\mu_r < 3$ for the Pareto distribution of runs) and with pauses ($\mu_p < 3$ for the Pareto distribution of pauses) can be fully consistent with the overall short displacements observed in our data (results not shown). The only possibility to truly discriminate between these alternatives would be to record movements at extremely high frequencies to see if long distance movements do occur. Importantly, we previously found that liver-localized memory CD8 T cells after 4 weeks post RAS immunization never made long distance jumps when recording was done at 3 frames/sec[19]. However, it is possible that long displacements may occur when liver-localized T cells detach from the endothelial wall and float with the blood flow as we observed with T cells after 1 week post RAS immunization (Fig. 2)[19]. Such movements, however, are better described as Levy flights and not Levy walks[22] because the speed at which T cells float with the blood in the liver dramatically exceeds average movement velocity of cells crawling on endothelium.

# Additional movies, figures, and tables

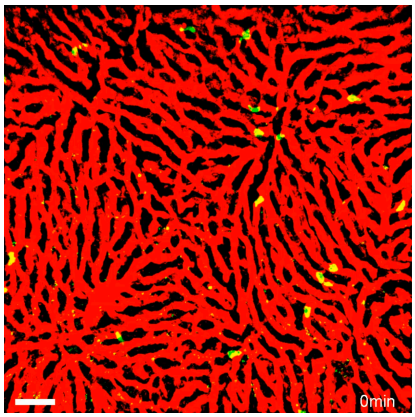


**Movie S1:** Example of movement of liver-localized CD8 T cells with labeled liver sinusoids. Experiments were performed as described in Fig. 1 in 3 individual mice. In the movie red denotes rhodamine dextran-labeled liver sinusoids and green are *Plasmodium*-specific liver-residence CD8 T cells. Cells turn yellow when there is an overlap between green and red. Bar scale is 50 $\mu$m. The volume of $512 \times 512 \times 44$ $\mu$m was scanned every 13 sec.

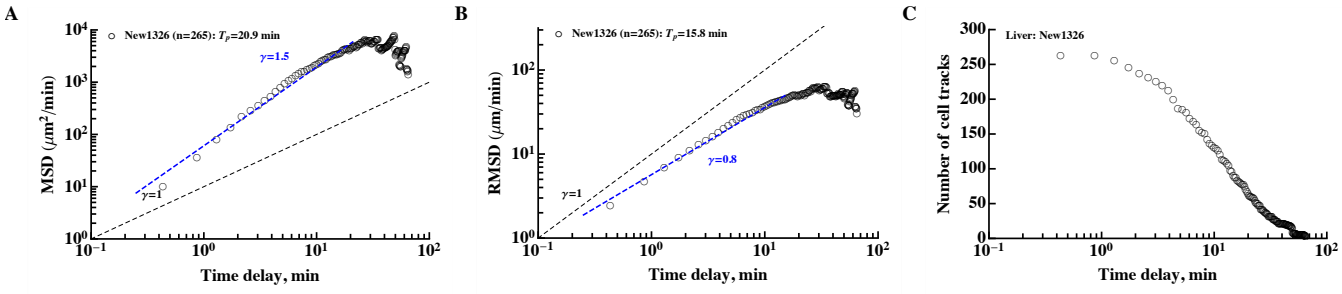


**Figure S1:** Departure from linear (on log-log scale) change in MSD or root mean squared displacement (RMSD) is in part due to decline in the number of cells with long tracks. For the New1326 datasets of activated CD8 T cells in the liver we calculated the MSD (panel A), RMSD (RMSD = $\sqrt{\text{MSD}}$, panel B), or the number of T cell tracks used to calculate these characteristics (panel C). Note that panel A lists a different slope from that given in Fig. 2A because different number of data points are taken into account in regression ($T_p$ is the persistence time defining which data points were taken for linear regression).

| Non scaled data | Dataset | Levy | Cauchy | GP | | Exp | H-N | Pareto | | Sampling |
|---|---|---|---|---|---|---|---|---|---|---|
| | | γ | γ | k | σ | λ | σ | rmin (μm) | μ-tail | frequency (sec) |
| Liver | New13 | 0.35 | 1.14 | -0.07 | 1.64 | 1.53 | 2.01 | 3.03 | 4.63 | 13.00 |
| Liver | New26 | 0.48 | 1.69 | 0.00 | 2.51 | 2.50 | 3.50 | 7.09 | 5.32 | 26.00 |
| Liver | New1326 | 0.49 | 1.69 | -0.01 | 2.51 | 2.49 | 3.46 | 7.09 | 5.47 | 26.00 |
| Liver | Wk1 | 0.13 | 0.40 | 0.28 | 0.50 | 0.76 | 2.15 | 0.61 | 2.55 | 6.50 |
| Liver | Wk4 | 0.10 | 0.33 | 0.01 | 0.46 | 0.46 | 0.66 | 0.94 | 4.42 | 3.25 |
| Liver | Lfa1_WT | 0.33 | 1.11 | 0.18 | 1.68 | 2.03 | 3.11 | 8.60 | 6.55 | 27.50 |
| Liver | Lfa1_KO | 0.18 | 0.57 | 0.11 | 0.80 | 0.91 | 1.46 | 2.10 | 3.30 | 27.50 |
| LN | 0209_Doc6 | 2.31 | 7.01 | -0.19 | 10.14 | 8.72 | 10.58 | 22.02 | 6.67 | 20.00 |
| LN | 0409_Doc7 | 1.20 | 3.67 | -0.48 | 5.77 | 4.16 | 4.71 | 6.14 | 6.74 | 20.00 |
| Scaled data | Dataset | Levy | Cauchy | General Pareto | | Exp | H-N | Pareto | | Sampling |
| | | γ | γ | k | σ | λ | σ | ρmin | μ-tail | frequency (sec) |
| Liver | New13 | 0.23 | 0.74 | -0.07 | 1.07 | 1.00 | 1.31 | 2.01 | 4.68 | 13.00 |
| Liver | New26 | 0.19 | 0.68 | 0.00 | 1.01 | 1.00 | 1.41 | 2.90 | 5.39 | 26.00 |
| Liver | New1326 | 0.20 | 0.68 | -0.01 | 1.01 | 1.00 | 1.39 | 2.91 | 5.55 | 26.00 |
| Liver | Wk1 | 0.17 | 0.52 | 0.28 | 0.66 | 1.00 | 2.82 | 0.78 | 2.52 | 6.50 |
| Liver | Wk4 | 0.22 | 0.71 | 0.01 | 0.99 | 1.00 | 1.44 | 1.93 | 4.28 | 3.25 |
| Liver | Lfa1_WT | 0.16 | 0.55 | 0.18 | 0.83 | 1.00 | 1.53 | 4.42 | 6.47 | 27.50 |
| Liver | Lfa1_KO | 0.20 | 0.63 | 0.11 | 0.88 | 1.00 | 1.60 | 2.29 | 3.30 | 27.50 |
| LN | 0209_Doc6 | 0.29 | 0.87 | -0.38 | 1.30 | 1.00 | 1.14 | 2.05 | 9.34 | 20.00 |
| LN | 0409_Doc7 | 0.29 | 0.88 | -0.48 | 1.39 | 1.00 | 1.13 | 1.55 | 7.00 | 20.00 |
| Structure | Dataset | Levy | Cauchy | GP | | Exp | H-N | Pareto | | |
| | | γ | γ | k | σ | λ | σ | rmin (μm) | μ-tail | |
| Liver sinusoids | Evans Blue | 3.48 | 10.54 | -0.20 | 15.71 | 13.38 | 16.37 | 36.36 | 7.45 | |
| LN FRCs | CCL19day5 | 2.31 | 7.01 | -0.19 | 10.14 | 8.72 | 10.58 | 22.02 | 6.67 | |

**Table S1:** Estimates of parameters providing best fits of various datasets. We fitted Levy (eqn. (S.6)), Cauchy (eqn. (S.4)), General Pareto (eqn. (S.7)), exponential (eqn. (S.8)), or half-normal (eqn. (S.5)) to the data on movement of T cells in the liver, lymph nodes, or to branch length distribution data for liver sinusoids or fibroblastic retricular cell (FRC) network in lymph nodes. For distribution with a location parameter $r_{\min}$ we set $r_{\min} = 0$. The same models were also fitted to scaled data (step length distribution data scaled by the RSMD). For imaging data we also list frequency of the imaging in the movies. See Extended Materials and Methods for the models and how models were fit to data.

| Non scaled data | Dataset | Levy | Cauchy | GP | Exp | H-N | Levy | Cauchy | GP | Exp | H-N |
|---|---|---|---|---|---|---|---|---|---|---|---|
| Liver | New13 | 11397 | 11433 | 7269 | 7302 | 7279 | 0.00 | 0.00 | 0.99 | 0.00 | 0.01 |
| Liver | New26 | 40929 | 41951 | 29623 | 29621 | 30631 | 0.00 | 0.00 | 0.32 | 0.68 | 0.00 |
| Liver | New1326 | 45728 | 46801 | 33002 | 33003 | 33968 | 0.00 | 0.00 | 0.58 | 0.42 | 0.00 |
| Liver | Wk1 | 5868 | 5968 | 2746 | 3398 | 6955 | 0.00 | 0.00 | 1.00 | 0.00 | 0.00 |
| Liver | Wk4 | 8184 | 8275 | 1860 | 1859 | 2575 | 0.00 | 0.00 | 0.39 | 0.61 | 0.00 |
| Liver | Lfa1_WT | 26909 | 28181 | 19649 | 19789 | 21556 | 0.00 | 0.00 | 1.00 | 0.00 | 0.00 |
| Liver | Lfa1_KO | 15307 | 15615 | 8554 | 8668 | 10549 | 0.00 | 0.00 | 1.00 | 0.00 | 0.00 |
| LN | 0209_Doc6 | 42313 | 41380 | 28946 | 30515 | 28685 | 0.00 | 0.00 | 0.00 | 0.00 | 1.00 |
| LN | 0409_Doc7 | 3352 | 3278 | 2281 | 2433 | 2281 | 0.00 | 0.00 | 0.53 | 0.00 | 0.47 |
| | Dataset | AIC | | | | | Akaike Weights | | | | |
| Scaled data | | Levy | Cauchy | GP | Exp | H-N | Levy | Cauchy | GP | Exp | H-N |
| Liver | New13 | 9219 | 9254 | 5090 | 5123 | 5099 | 0.00 | 0.00 | 0.99 | 0.00 | 0.01 |
| Liver | New26 | 26806 | 27820 | 15491 | 15489 | 16494 | 0.00 | 0.00 | 0.32 | 0.68 | 0.00 |
| Liver | New1326 | 30021 | 31086 | 17287 | 17287 | 18248 | 0.00 | 0.00 | 0.59 | 0.41 | 0.00 |
| Liver | Wk1 | 7141 | 7242 | 4020 | 4673 | 8231 | 0.00 | 0.00 | 1.00 | 0.00 | 0.00 |
| Liver | Wk4 | 14498 | 14595 | 8181 | 8180 | 8901 | 0.00 | 0.00 | 0.41 | 0.59 | 0.00 |
| Liver | Lfa1_WT | 18723 | 19988 | 11456 | 11596 | 13359 | 0.00 | 0.00 | 1.00 | 0.00 | 0.00 |
| Liver | Lfa1_KO | 16191 | 16499 | 9439 | 9554 | 11435 | 0.00 | 0.00 | 1.00 | 0.00 | 0.00 |
| LN | 0209_Doc6 | 24765 | 23829 | 11394 | 12965 | 11133 | 0.00 | 0.00 | 0.00 | 0.00 | 1.00 |
| LN | 0409_Doc7 | 1924 | 1849 | 853 | 1005 | 853 | 0.00 | 0.00 | 0.54 | 0.00 | 0.46 |
| Structure | Dataset | Levy | Cauchy | GP | Exp | H-N | Levy | Cauchy | GP | Exp | H-N |
| Liver sinusoids | Evans Blue | 47544 | 47114 | 37936 | 38375 | 37599 | 0.00 | 0.00 | 0.00 | 0.00 | 1.00 |
| LN FRCs | CCL19day5 | 29759 | 29402 | 23058 | 23349 | 22758 | 0.00 | 0.00 | 0.00 | 0.00 | 1.00 |

**Table S2:** AIC values and Akaike weights of alternative models fit to different datasets (as described in Tab. S1). See Extended Materials and Methods for the models and how models were fit to data.

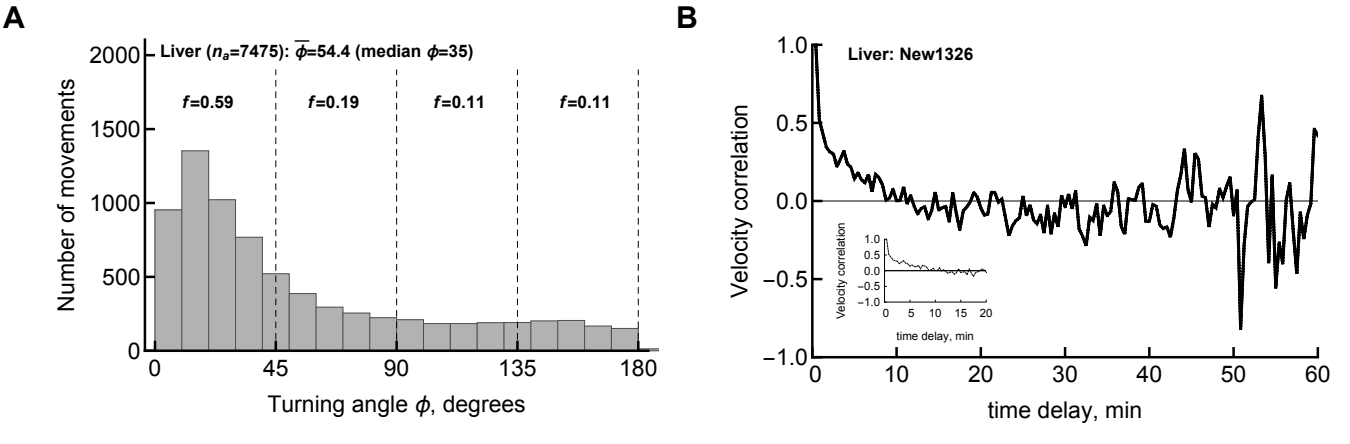


**Figure S2:** Activated CD8 T cells in the liver perform correlated random walk with a high degree of persistence. A: For every track in our dataset that includes measurement of T cell movement in the liver at 26 sec time steps, we calculated the turning angles for each subsequent cell movement. The data are from 3 individual mice involving 268 tracks and 7,475 movements ("New1326" dataset). Fraction $f$ denotes the frequency of turning angles between specific cutoff values. B: We calculated the correlation between vectors determining the first movement and every another movement for all 268 cell tracks in our data. Specifically, we calculated the angle $\phi$ between the vector determining the first cell movement and every another movement at different times and plotted $\cos(\phi)$ vs. the time difference between first movement and another movements. Insert in B shows the data for the first 20 min of imaging.

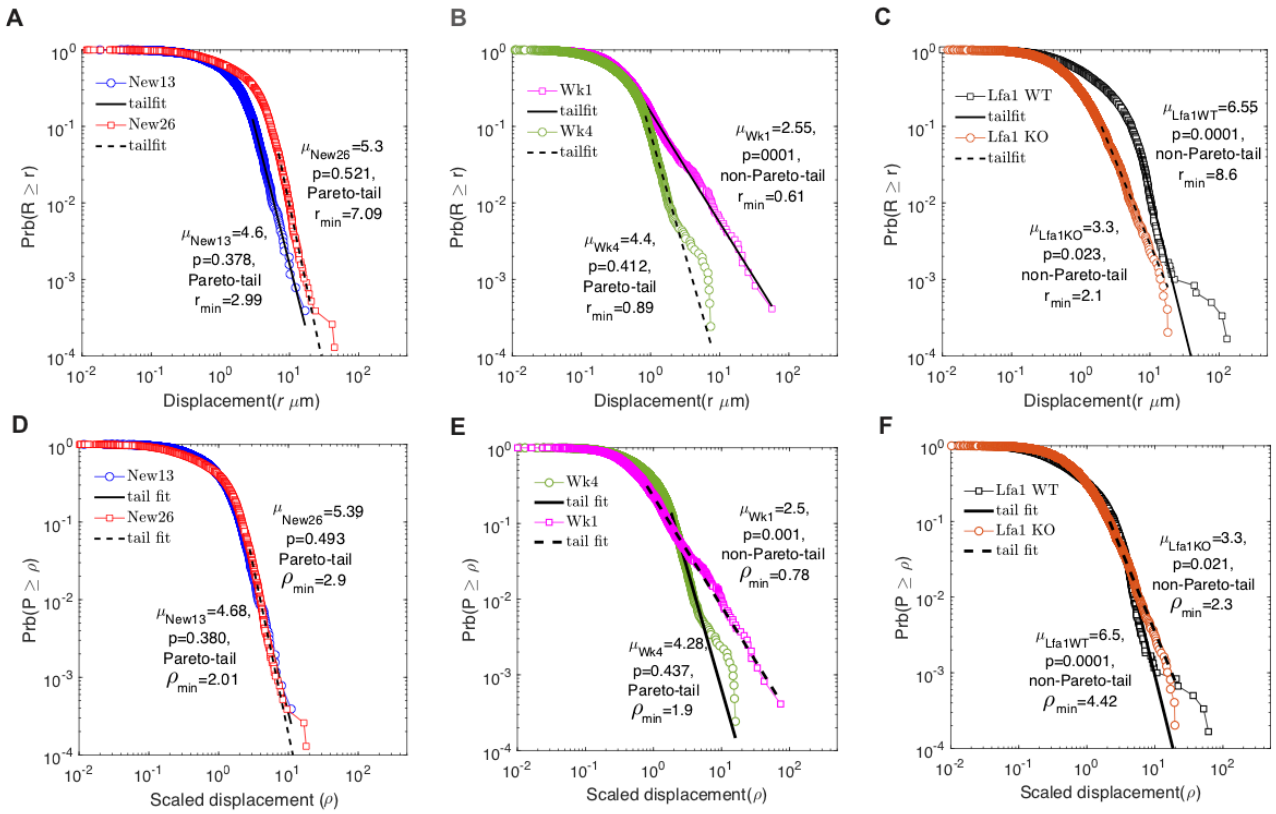


**Figure S3:** Fits of the Pareto (powerlaw) distributions to the CD8 T cell in the liver displacement data. We used previously published method[23] to estimate the shape parameter $\mu$ of the Pareto distribution (eqn. (S.9)) for 6 different datasets (see Materials and Methods for dataset description) by fitting a linear function (on log-log scale) to the tails of the data distribution using likelihood method. We fit the model to actual displacements $r$ (A-C) or to scaled displacements $\rho$ (D-F). The cut-off $r_{\min}$ (for actual displacements) or $\rho_{\min}$ (for normalized displacements) for the linear regressions was chosen using a goodness-of-fit based method[23]. In short, for multiple choices of $r_{\min}$ slope $\mu$ was estimated via the method of maximum likelihood and the Kolmogorov-Smirnov goodness of fit statistic, $D$, was calculated. Value of $r_{\min}$ that resulted in minimal fit statistics $D$ was chosen for the final fit. Indicated $p$ values were estimated by resampling the data 1000 times and performing Kolmogorov-Smirnov Goodness of Fit Test[23].

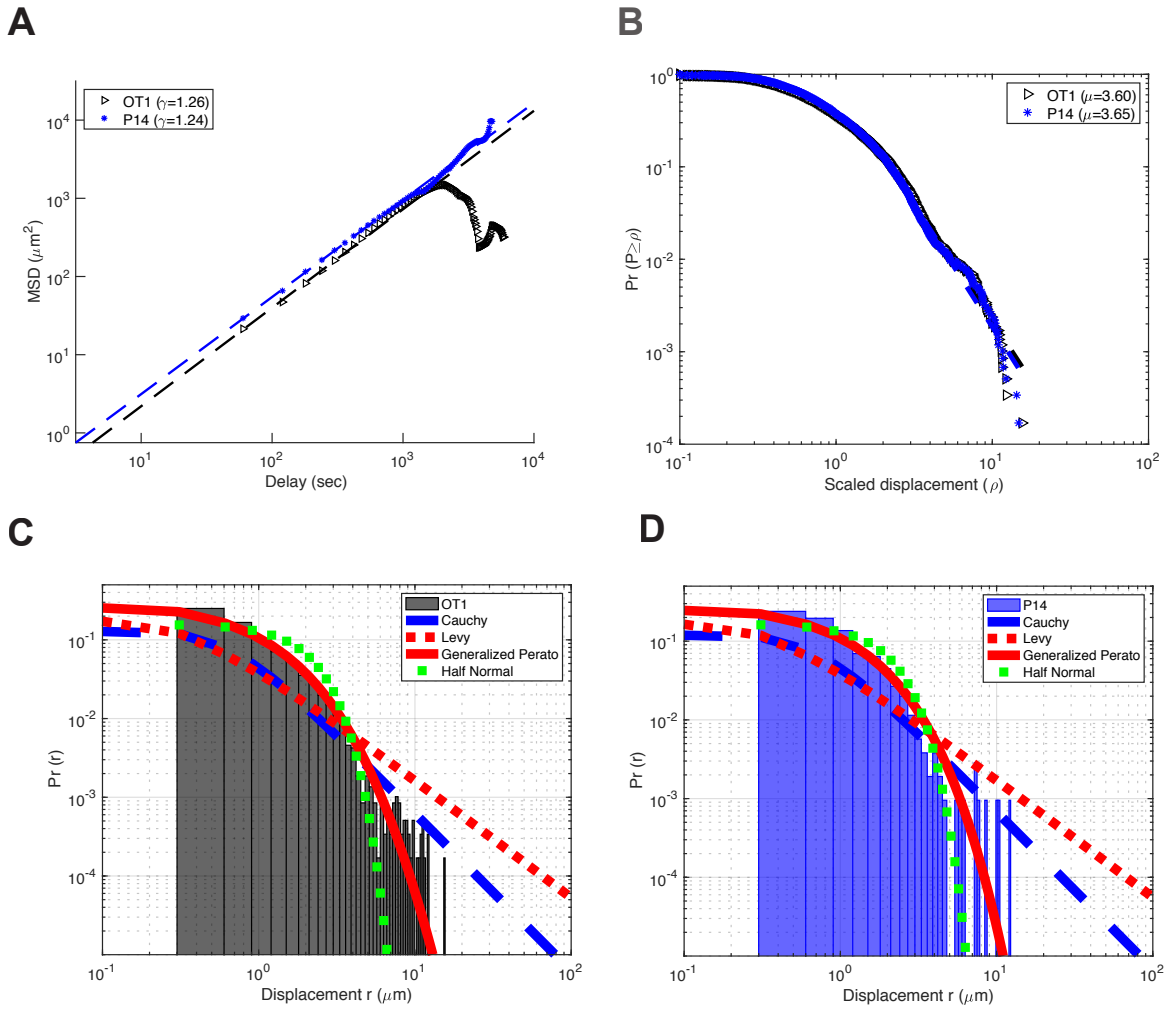


**Figure S4:** Activated CD8 T cells are superdiffusive Brownian walkers in the liver during *Plasmodium* infection. We performed experiments in which *in vitro* activated OT-I (*Plasmodium berghei*-specific) and P14 (LCMV-specific) CD8 T cells were transferred i.v. into naive mice and these mice were 1.5-2 hours later infected with $10^5$ *Plasmodium berghei*-CS$^{5M}$ sporozoites expressing SIINFEKL epitope from chicken ovalbumin [19,36]. Ten to twenty minutes after infection, livers of infected mice were exposed and movements of T cells were recorded using intravital microscopy [37]. We performed the same analyses as in the main text (Fig. 2) including (A) regression analysis of the MSD with time, (B) distribution of movement lengths, (C)-(D) fitting alternative distributions to the movement data for OT1 (C) or P14 (D) T cells. Generalized Pareto distribution was best describing data in C-D (results not shown).

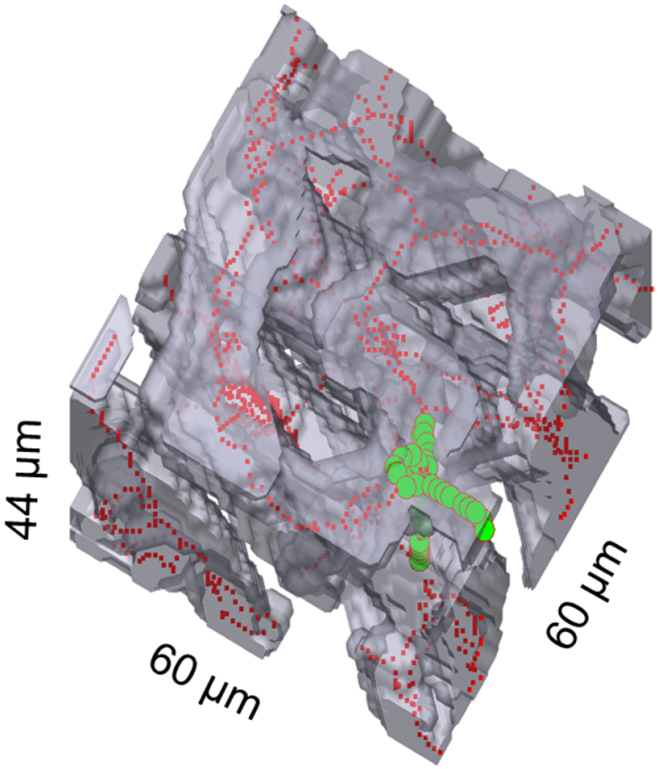


**Figure S5:** Example of the simulation in which T cells were moving in sinusoids of the liver. Grey denotes sinusoids, red dots denote the mean path of the sinusoids, and green denotes moving T cell.

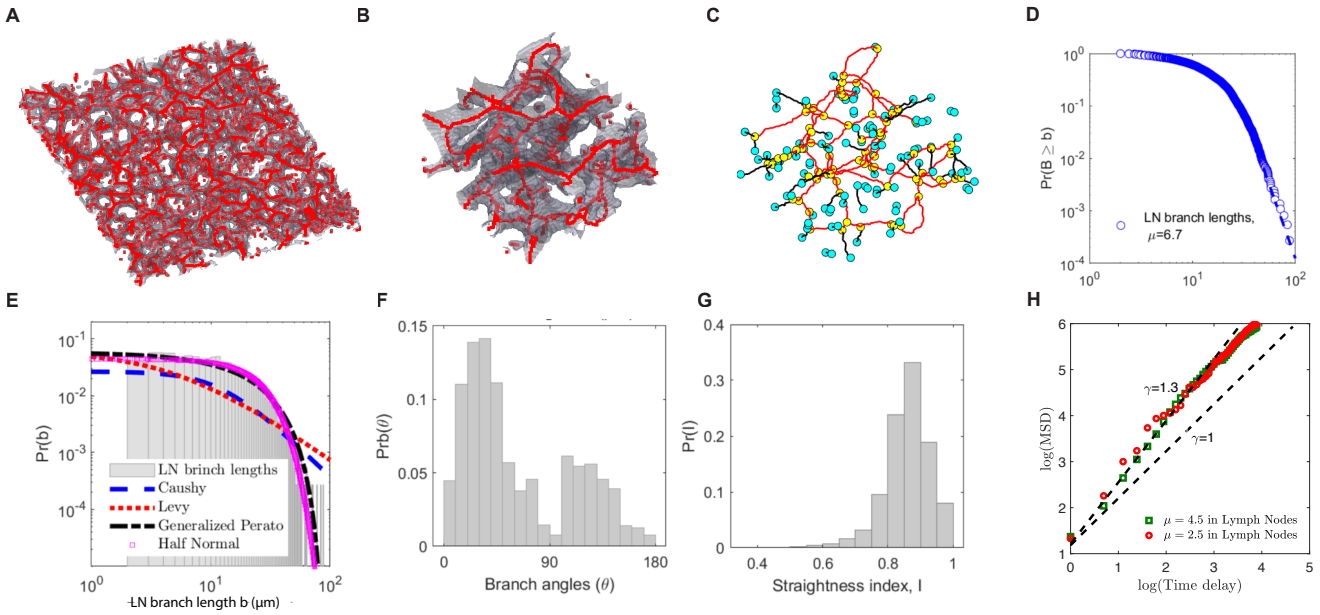


**Figure S6:** Characterizing structure of the fibroblastic reticular cell network in the murine lymph nodes. We used previously published data in which FRCs were imaged using Ccl19$^{\text{eyfp}}$ reporter mouse[28]. As with analysis of liver sinusoids z-stacks of LN images were contrasted and mean paths in the FRCs were calculated. To simulate T cell walk on digitized FRC network we assumed that movement length distribution is described by the powerlaw (Pareto) distribution with $r_{\min} = 0.2$ $\mu$m and $\mu = 4.5$ (for Brownian walks) or $\mu = 2.5$ (for Levy walks).

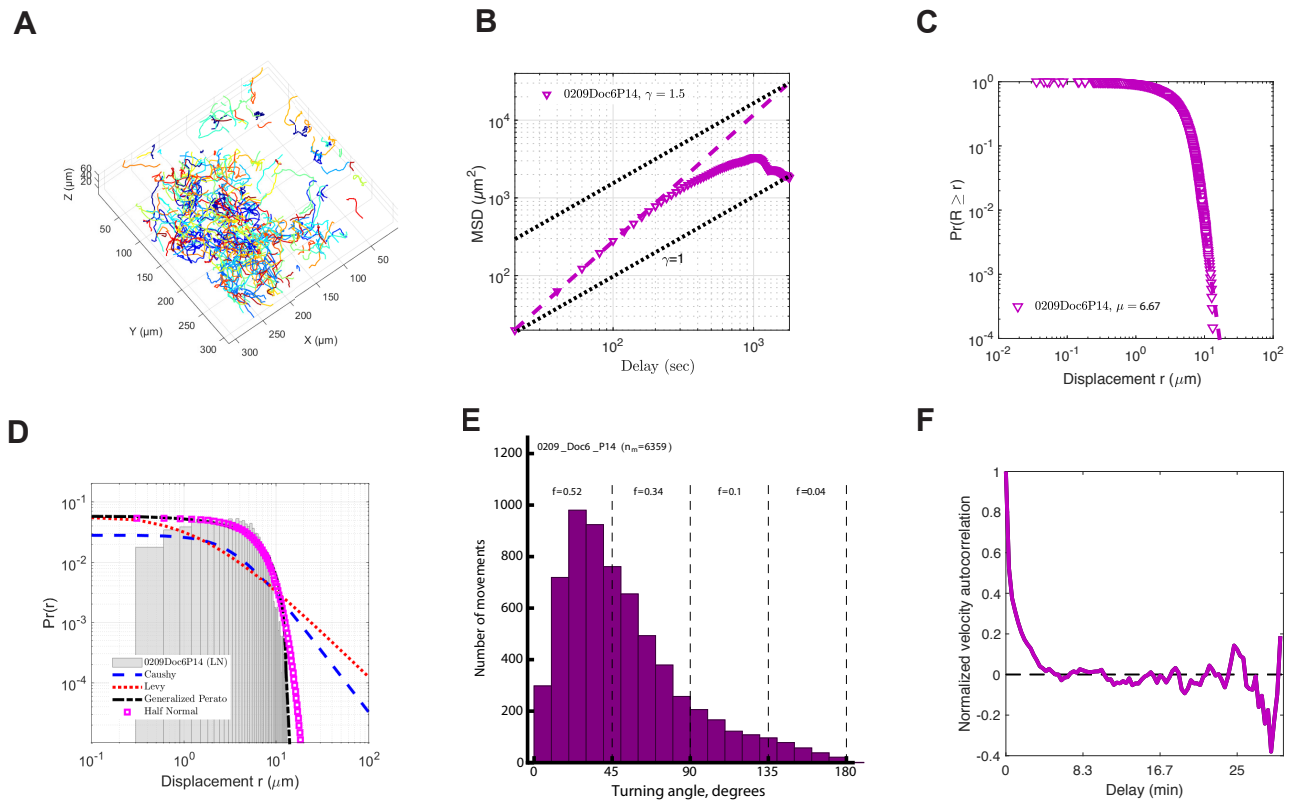


**Figure S7:** Naive CD8 T cells in lymph nodes are not superdiffusive. We analyzed experimental data in which naive CD8 T cells moving in resting lymph nodes were imaged using two photon microscope[28]. Example of the analysis of data from one of 6 such datasets is show. A: individuals tracks of T cells digitized using Imaris software; B: MSD vs. time for all T cels indicating short-term (2-3 min) persistence/superdiffusion; C: movement length distribution with tail analysis performed[23]; D: fits of several alternative distributions to the movement length distribution data; E: distribution of turning angles of T cells in the LNs; F: velocity autocorrelation function for T cells moving in the LNs.

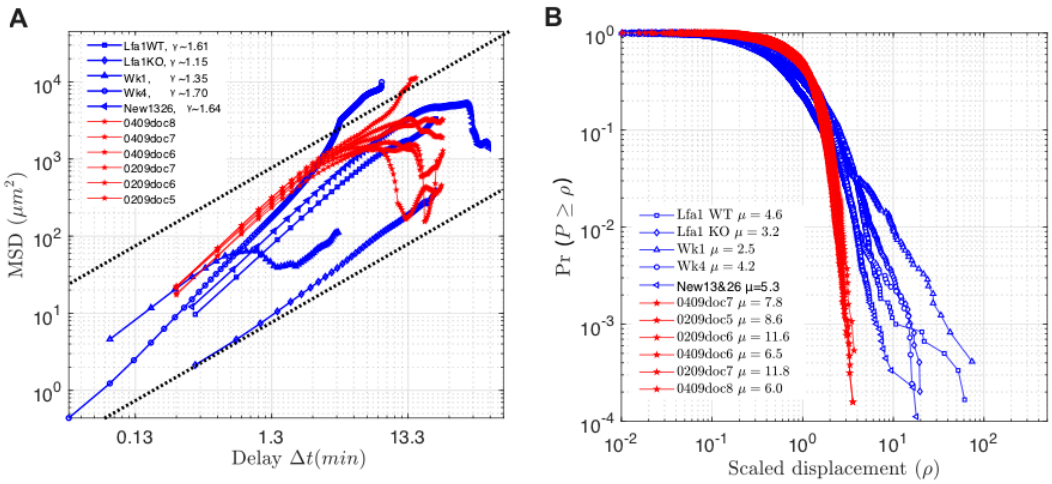


**Figure S8:** T cells in the liver display persistent movement for a longer time as compared to T cells in the LNs. Data from all datasets on movement of activated CD8 T cells in the liver (blue) or naive CD8 T cells in the LNs (red) are plotted together. A: difference in MSD for T cells in the LNs vs. liver; B: difference in movement length distribution of T cells in the liver vs. LNs.

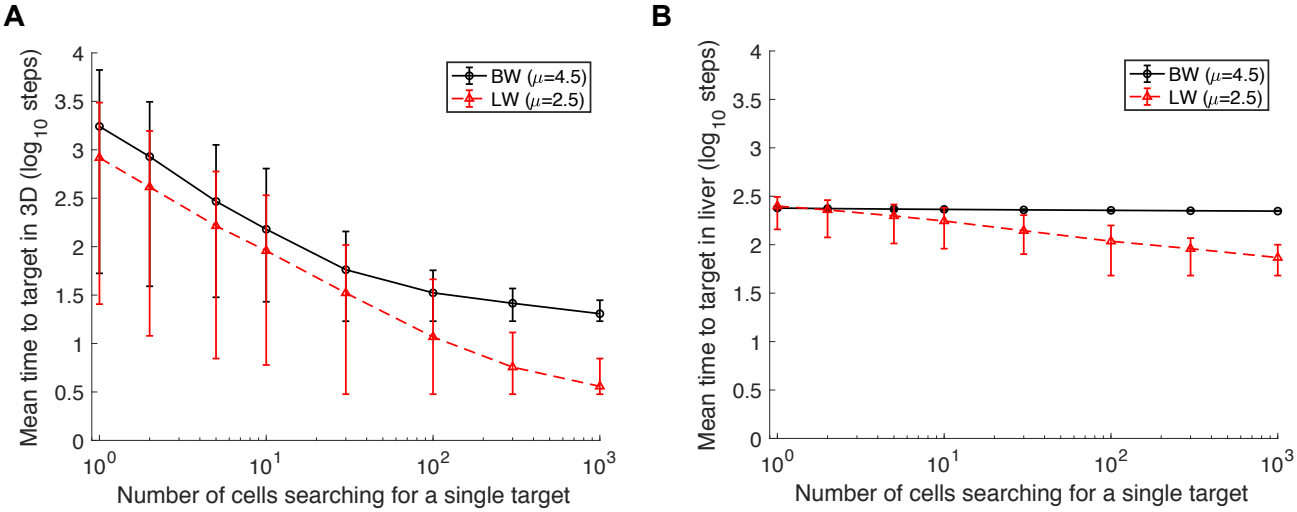


**Figure S9:** Benefits of Levy walks depend on the environment (open space/3D vs. liver/1D) and the number of T cells $n$ searching for the infection site. We simulated T cells searching for an infection similar to that in Fig. 5 either in free 3D space (panel A, starting at 100$\mu$m from the target) or in the liver sinusoids (panel B, starting at 500$\mu$m from the target) assuming that there are different numbers of T cells all independently searching for the infection. For each simulation the time to target was calculated as the minimal time to find the targeted by any T cell in $n$ cells. Brownian walks (BW) were described by the Pareto distribution with $\mu = 4.5$ and Levy walks (LW) were described with $\mu = 2.5$ (eqn. (S.9)). In both cases, the average step length distribution was set to $\bar{r} = 2.1$ $\mu$m per time step. Error bars denote 95% range for the estimated time to target. A given T cell reaches the target when it is within 40$\mu$m from the target[34,35].